

# A central WENO scheme for solving hyperbolic conservation laws on non-uniform meshes

G. Capdeville\*

*Ecole Centrale de Nantes, Laboratoire de Mécanique des Fluides, 1, rue de la Noë, B.P. 92101, 44321 Nantes cedex 3, France*

Received 26 January 2007; received in revised form 11 July 2007; accepted 23 November 2007

Available online 4 December 2007

---

## Abstract

This paper proposes a new WENO procedure to compute multi-scale problems with embedded discontinuities, on non-uniform meshes.

In a one-dimensional context, the WENO procedure is first defined on a five-points stencil and designed to be fifth-order accurate in regions of smoothness. To this end, we define a finite-volume discretization in which we consider the cell averages of the variable as the discrete unknowns. The reconstruction of their point-values is then ensured by a unique fifth-order polynomial. This optimum polynomial is considered as a symmetric and convex combination, by ideal weights, of four quadratic polynomials.

The symmetric nature of the resulting interpolation has an important consequence: the choice of ideal weights has no influence on the accuracy of the discretization. This advantage enables to formulate the interpolation for non-uniform meshes. Following the methodology of the classic WENO procedure, non-oscillatory weights are then calculated from the ideal weights.

We adapt this procedure for the non-linear weights to maintain the theoretical convergence properties of the optimum reconstruction, whatever the problem considered.

The resulting scheme is a fifth-order WENO method based on central interpolation and TVD Runge–Kutta time-integration. We call this scheme the CWENO5 scheme.

Numerical experiments in the scalar and the 1D Euler cases make it possible to check and to validate the options selected. In those experiments, we emphasize the resolution power of the method by computing test cases that model realistic aero-acoustic problems. Finally, the new algorithm is directly extended to bi-dimensional problems.

© 2007 Elsevier Inc. All rights reserved.

**Keywords:** Non-linear aeroacoustics; Central WENO interpolation; Hyperbolic systems; Non-uniform meshes; Two-dimensional Riemann problem

---

---

\* Tel.: +33 2 4037 1651; fax: +33 2 4037 2523.

E-mail address: [guy.capdeville@ec-nantes.fr](mailto:guy.capdeville@ec-nantes.fr)

## 1. Introduction

Nowadays, high-order computational methods are highly demanded for solving problems in computational fluid dynamics (CFD). For flow problems with intricate structures and a very broad range of characteristic scales, high resolution is necessary for the structural information to be correctly extracted.

For example, in the direct numerical simulation (DNS) and the large eddy simulation (LES) of turbulence, it is required that the numerical schemes be highly accurate. Computational aero-acoustics (CAA) is another area where high-resolution schemes are required. Moreover, if the flow fields involve shock waves, these schemes should also be non-oscillatory near the discontinuities without leading to an excessive damping of the turbulent or acoustic fluctuations.

Weighted essentially non-oscillatory (WENO) schemes are one class of high-order numerical schemes. Historically, WENO schemes are based upon the successful essentially non-oscillatory (ENO) schemes that started with the henceforth-classic paper of Harten et al. in 1987 [1].

WENO schemes improve upon ENO schemes in robustness, smoothness of the numerical fluxes, convergence properties and computational efficiency. Owing to these advantages, a large variety of WENO schemes was designed in recent years; see [2] for a good overview.

Nevertheless, in spite of a vast field of application, classical WENO schemes suffer from two genuine drawbacks.

The essential idea in the WENO methodology is a linear combination of lower order reconstructions to obtain a higher-order approximation. The combination coefficients, also called linear weights or ideal weights, are obtained by local geometry of the mesh and order of accuracy. When the grid is uniform or is smoothly varying, the linear weights remain positive. However, for general geometries that cannot be covered by a Cartesian grid, these weights may become negative. Unfortunately, WENO procedures cannot be applied directly to obtain a monotone scheme if negative linear weights are present [2].

This is the first significant drawback related to a procedure WENO.

A Previous strategy for handling this difficulty was to get rid of the negative linear weights by either regrouping of stencils [4], or reducing the order of accuracy [5]. Another possible solution is to use a splitting technique to treat the negative weights, without the necessity to get rid of them [3]. Even if they proved to be efficient, these solutions complicate the resulting algorithm.

Although less significant, the second drawback of a WENO scheme is related to its actual rate of convergence. Indeed, despite the high order convergence behaviour often exhibited by WENO schemes, their actual rate of convergence is less than the optimum order for many problems [6,7]. To calculate the non-linear weights that ensure the non-oscillatory properties of the scheme, a classical WENO procedure necessitates specifying the magnitude of  $\varepsilon$ , a small parameter initially designed to keep the weights bounded [2]. However,  $\varepsilon$  appears as a dimensional quantity in the formulation of the non-linear weights. Thus,  $\varepsilon$  must be normally selected on a case-by-case basis, which belies on the fact that  $\varepsilon$  changes the order of convergence. This property, combined with the level of grid resolution, has a dramatic effect on the convergence of WENO schemes [6].

A strategy to circumvent this problem is to define an appropriate scaling [7], or to map the non-oscillatory weights to values such that the optimal conditions on the weights are satisfied [6].

In this paper, we propose a new approach to effectively deal with these drawbacks without resorting to complex strategies or limiting the generality of a WENO procedure.

In a finite-volume framework, we construct a fifth-order non-oscillatory scheme for solving 1D non-linear hyperbolic systems of conservation laws. This scheme lies upon a central and local WENO interpolation: we call this scheme the CWENO5 scheme.

To generate such a scheme, we use and extend the ideas of Levy et al. [8]. In their paper, the authors introduced a new central weighted non-oscillatory (CWENO) reconstruction. This new reconstruction is based on defining a suitable quadratic function that is added to linear polynomials to obtain third-order accuracy in smooth regions. In regions with discontinuities or large gradients, the weights are changed automatically and smoothly so that they switch to a one-sided second-order linear reconstruction. This reconstruction turns out to be extremely compact; in the one-dimensional case, the reconstruction is based on a three-point stencil. The main advantage of this procedure is that the choice of ideal weights has no influence on the properties of

discretization. Any symmetric choice of the constants defining the ideal weights will provide the desired accuracy. This property must be contrasted with classical upwind WENO schemes.

To maintain this property and to generalize the WENO procedure to fifth-order accuracy on non-uniform meshes, we develop a specific non-oscillatory fifth-order reconstruction based on a five-points stencil. For this purpose, four polynomials are defined: three quadratic polynomials based on three-points stencils are first calculated. These three-points stencils are extracted from the optimum five-points stencil. The fourth polynomial is a second-order central polynomial based on the five-points stencil. This latter polynomial is calculated starting from the difference between the optimum polynomial and the convex combination of the three second-order polynomials previously calculated. The central polynomial is only necessary for the accurate recovery of the point-values in regions of smoothness. When a discontinuity appears into the solution, this polynomial is automatically removed by the procedure.

Thus, the optimum polynomial defined on the five-points stencil is considered as a linear and convex combination, by ideal and symmetric weights, of these polynomials.

To end the description of the non-oscillatory reconstruction, the formulation of the non-linear weights is specified.

To reduce the influence of the parameter  $\varepsilon$  on the convergence properties of the scheme, we replace this parameter by a new function that depends on the solution. This operation is accomplished by using the information brought by the local smoothness indicators.

Comparing with the original scheme of Shu (UWENO5) [2], we can stress the following differences:

- The ideal weights are symmetric and free of the regularity of the mesh. Consequently, the scheme remains monotone even on a non-uniform grid.
- The function that replaces the parameter  $\varepsilon$  not only ensures the integrity of the non-oscillatory weights, but is also designed to preserve the theoretical convergence properties of the reconstruction in regions of smoothness.

This paper is organized as follows: we start in Section 2 by detailing the construction and implementation of the CWENO5 scheme, for 1D scalar and 1D Euler equations. The reconstruction is defined on non-uniform meshes; the specific procedure to generate a non-oscillatory reconstruction is then emphasized. The function that replaces the parameter  $\varepsilon$  is then detailed and discussed. In the case of a uniform mesh, we provide the coefficients to calculate the interpolation.

In Section 3 we select numerical tests to validate the method. Asymptotic analysis stability is first managed to check the influence of the boundary conditions, the stretching of the mesh and possible source terms. First, the scheme is tested by computing solutions of scalar non-linear and 1D Euler equations. Emphasis is put on the resolution power of the method by computing cases that model realistic aero-acoustic configurations. Lastly, the new algorithm is naturally extended to bi-dimensional Cartesian problems and validated by solving academic bi-dimensional Riemann problems.

## 2. Non-oscillatory reconstruction: the CWENO5 scheme

### 2.1. Governing equations

Let the following scalar non-linear hyperbolic problem be defined over the domain,  $\Omega$ :

$$\begin{cases} u_t + f(u)_x = 0 & \forall x \in \Omega, \\ u(x, t = 0) = u_o(x). \end{cases} \quad (1)$$

Defining the discrete cell  $I_i \equiv [x_{i-1/2}, x_{i+1/2}]$ ,  $\Omega$  is partitioned in  $N$  non-overlapping cells:  $\Omega = \bigcup_{i=1}^N I_i$ . The non-uniform cell size is calculated as  $\Delta x_i \equiv x_{i+1/2} - x_{i-1/2}$ . Lastly, we define the discrete cell averages of  $u$  as  $\bar{u}_i \equiv \frac{1}{\Delta x_i} \int_{I_i} u(x, t) dx$ .

Following the finite-volume methodology for generating an upwind scheme, the fluxes for  $u$  are approximated according to the classical formula:

$$\begin{cases} \tilde{f}_{i+1/2} = f(u_{i+1/2}^L) + a_{i+1/2}^- \times (u_{i+1/2}^R - u_{i+1/2}^L) \\ \text{with : } a_{i+1/2} \equiv \begin{cases} \frac{f(u_{i+1/2}^R) - f(u_{i+1/2}^L)}{u_{i+1/2}^R - u_{i+1/2}^L} & \text{if } u_{i+1/2}^R \neq u_{i+1/2}^L \\ f'(u_{i+1/2}^L) & \text{otherwise} \end{cases} \end{cases} \quad (2)$$

In the numerical tests that we carried out, no entropy correction proved to be necessary.

Then, the discretization of the spatial operator generates an ODE in time for the discrete unknowns  $\bar{u}_i$ . This ODE is integrated by a third-order TVD Runge–Kutta scheme (TVD RK3) initially developed by Shu and Osher [15].

## 2.2. Reconstruction from cell-averages, $\bar{u}_i$

To begin, we select an optimal polynomial of degree 4, denoted by  $\tilde{u}_{\text{opt}}(x)$ , on the central stencil  $\{I_{i-2}, I_{i-1}, I_i, I_{i+1}, I_{i+2}\}$ , (see Fig. 1):  $\tilde{u}_{\text{opt}}(x) \equiv \sum_{j=1}^5 a_{j-1} (x - x_i)^{j-1}$ .

Following [1],  $\tilde{u}_{\text{opt}}(x)$  is uniquely defined by the relations:

$$\frac{1}{\Delta x_{i+k}} \int_{I_{i+k}} \tilde{u}_{\text{opt}}(x) dx = \bar{u}_{i+k}, \quad k \in \{-2, -1, 0, 1, 2\}. \quad (3)$$

Thus, we generated a linear system for the undetermined coefficients  $\{a_j\}$ .

This system can be re-written as

$$\mathbf{U} = \mathbf{C} \times \mathbf{A} \quad (4)$$

with the following notations:

$$\mathbf{U} \equiv [\bar{u}_{i-2}, \bar{u}_{i-1}, \bar{u}_i, \bar{u}_{i+1}, \bar{u}_{i+2}]^t,$$

$$\mathbf{A} \equiv [a_j]_{j \in \{0, \dots, 4\}}^t,$$

$$\mathbf{C} \equiv \begin{cases} c_{1j} = \frac{(-1)^j}{j \Delta x_{i-2}} \left[ (\Delta x_{i-1} + \frac{\Delta x_i}{2})^j - (\Delta x_{i-1} + \Delta x_{i-2} + \frac{\Delta x_i}{2})^j \right], \\ c_{2j} = \frac{(-1)^j}{j \Delta x_{i-1}} \left[ (\frac{\Delta x_i}{2})^j - (\Delta x_{i-1} + \frac{\Delta x_i}{2})^j \right], \\ c_{3j} = \frac{(\Delta x_i)^{j-1}}{j 2^j} (1 + (-1)^{j+1}) \quad j \in \{1 \dots 5\}, \\ c_{4j} = \frac{1}{j \Delta x_{i+1}} \left[ (\Delta x_{i+1} + \frac{\Delta x_i}{2})^j - (\frac{\Delta x_i}{2})^j \right], \\ c_{5j} = \frac{1}{j \Delta x_{i+2}} \left[ (\Delta x_{i+2} + \Delta x_{i+1} + \frac{\Delta x_i}{2})^j - (\Delta x_{i+1} + \frac{\Delta x_i}{2})^j \right]. \end{cases}$$

For solving the Riemann's problem that arises at each interface, we only need the approximations to the values of  $u(x)$  at the cell boundaries.

These values are calculated according to the relation:

$$u_{i+1/2}^L = ({}^t \mathbf{D} \times \mathbf{C}^{-1}) \times \mathbf{U} \equiv \sum_{j=1}^5 \tilde{a}_j \bar{u}_{i+j-3} \quad (5)$$

with the following definition:  $\mathbf{D} \equiv \left[ \left( \frac{\Delta x_i}{2} \right)^{j-1} \right]_{j=1, \dots, 5}$

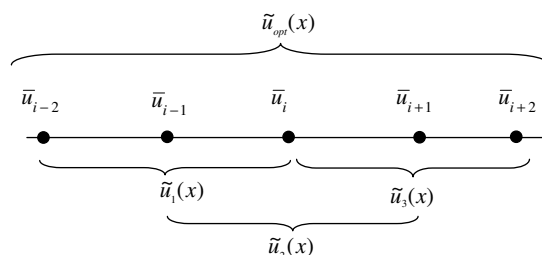


Fig. 1. Discrete stencils for the CWENO5 procedure.

The constants  $\{\tilde{a}_j\}$  depend on the cell sizes,  $\Delta x_i$ , but not on the function  $u$  itself. Practically, these constants are pre-computed in the case of a non-uniform grid and stored before solving the PDEs.

For the calculations of  $u_{i+1/2}^R$ , the constants  $\{\tilde{a}_j\}$  are simply calculated by modifying the form of the vector  $\mathbf{D}$ :

$$\mathbf{D} \equiv \left[ (-1)^{j+1} \left( \frac{\Delta x_i}{2} \right)^{j-1} \right]_{j=1, \dots, 5}.$$

When the grid is uniform,  $\Delta x_i \equiv \Delta x$ , the expressions for the polynomial coefficients,  $a_j$ , do not depend on the points of discretization anymore. In such a case, these expressions can be explicitly formulated to fully determine  $\tilde{u}_{\text{opt}}(x)$  and, later, the smoothness indicators:

$$\begin{cases} a_0 = \frac{1067}{960} \bar{u}_i - \frac{29}{480} (\bar{u}_{i+1} + \bar{u}_{i-1}) + \frac{3}{640} (\bar{u}_{i+2} + \bar{u}_{i-2}), \\ 48\Delta x \times a_1 = 34(\bar{u}_{i+1} - \bar{u}_{i-1}) + 5(\bar{u}_{i-2} - \bar{u}_{i+2}), \\ -16\Delta x^2 \times a_2 = \bar{u}_{i-2} + 22\bar{u}_i + \bar{u}_{i+2} - 12(\bar{u}_{i+1} + \bar{u}_{i-1}), \\ -12\Delta x^3 \times a_3 = 2(\bar{u}_{i+1} - \bar{u}_{i-1}) + (\bar{u}_{i-2} - \bar{u}_{i+2}), \\ 24\Delta x^4 \times a_4 = \bar{u}_{i-2} + 6\bar{u}_i + \bar{u}_{i+2} - 4(\bar{u}_{i+1} + \bar{u}_{i-1}). \end{cases} \quad (6)$$

Finally, the calculated point-values at the cell boundary  $x = x_{i+1/2}$  are such that

$$u_{i+1/2} \equiv \tilde{u}_{\text{opt}}(x_{i+1/2}) = u(x_{i+1/2}) + \mathcal{O}(\Delta x^5) \quad (7)$$

To derive an essentially non-oscillatory reconstruction, we need to define three supplementary polynomials ( $\tilde{u}_1(x)$ ,  $\tilde{u}_2(x)$ ,  $\tilde{u}_3(x)$ ), approximating  $u(x)$  with a lower accuracy on  $I_i$ .

Thus, we define the polynomial of second-order accuracy,  $\tilde{u}_1(x)$ , on the reduced stencil  $\{I_{i-2}, I_{i-1}, I_i\}$ ,  $\tilde{u}_2(x)$  is defined on the stencil  $\{I_{i-1}, I_i, I_{i+1}\}$ , whereas  $\tilde{u}_3(x)$  is defined on the stencil  $\{I_i, I_{i+1}, I_{i+2}\}$  (see Fig. 1).

When the grid is non-uniform, we strictly follow the procedure previously explained. Now, we have to invert a  $3 \times 3$  linear system similar to (4) for the unknown coefficients  $\{a_j\}$ ,  $j \in \{0, \dots, 2\}$ , defining  $\tilde{u}_1(x)$ ,  $\tilde{u}_2(x)$  and  $\tilde{u}_3(x)$ .

Once again, the constants determining the interpolation are pre-computed and stored before solving the PDEs.

When the grid is uniform, the values of the coefficients for  $\tilde{u}_1(x)$ ,  $\tilde{u}_2(x)$  and  $\tilde{u}_3(x)$  can be explicitly formulated.

For  $\tilde{u}_1(x)$  defined on  $\{I_{i-2}, I_{i-1}, I_i\}$ , we have

$$\begin{cases} a_0 = \frac{23}{24} \bar{u}_i + \frac{1}{12} (\bar{u}_{i-1} - \frac{1}{2} \bar{u}_{i-2}), \\ 2\Delta x \times a_1 = 3\bar{u}_i - 4\bar{u}_{i-1} + \bar{u}_{i-2}, \\ 2\Delta x^2 \times a_2 = \bar{u}_i - 2\bar{u}_{i-1} + \bar{u}_{i-2}. \end{cases} \quad (8)$$

For  $\tilde{u}_2(x)$  defined on  $\{I_{i-1}, I_i, I_{i+1}\}$ :

$$\begin{cases} a_0 = \frac{13}{12} \bar{u}_i + \frac{1}{24} (\bar{u}_{i-1} + \bar{u}_{i+1}), \\ 2\Delta x \times a_1 = (\bar{u}_{i+1} - \bar{u}_{i-1}), \\ 2\Delta x^2 \times a_2 = \bar{u}_{i+1} - 2\bar{u}_i + \bar{u}_{i-1}. \end{cases} \quad (9)$$

And for  $\tilde{u}_3(x)$  defined on  $\{I_i, I_{i+1}, I_{i+2}\}$ :

$$\begin{cases} a_0 = \frac{23}{24} \bar{u}_i + \frac{1}{12} (\frac{1}{2} \bar{u}_{i+1} - \bar{u}_{i+2}), \\ -2\Delta x \times a_1 = 3\bar{u}_i - 4\bar{u}_{i+1} + \bar{u}_{i+2}, \\ 2\Delta x^2 \times a_2 = \bar{u}_i - 2\bar{u}_{i+1} + \bar{u}_{i+2}. \end{cases} \quad (10)$$

### 2.3. Essentially non-oscillatory reconstruction

If the discrete stencil defining  $\tilde{u}_{\text{opt}}(x)$  contains a discontinuity or large gradients, spurious oscillations can appear in the numerical solution. To avoid such a problem we construct a WENO procedure that smoothly adapts the stencil in the neighbourhood of the singularity.

Defining the non-oscillatory reconstruction on  $I_i$  by  $\tilde{u}^i(x)$ , we want the following properties to be verified:

$$\tilde{u}^i(x) = \begin{cases} \tilde{u}_{\text{opt}}(x) & \text{if the stencil } \{I_{i-2}, I_{i-1}, I_i, I_{i+1}, I_{i+2}\} \text{ is in the smooth regions,} \\ \tilde{u}_1(x) & \text{if the solution is not smooth and } \{I_{i-2}, I_{i-1}, I_i\} \text{ is in the smooth region,} \\ \tilde{u}_2(x) & \text{if the solution is not smooth and } \{I_{i-1}, I_i, I_{i+1}\} \text{ is in the smooth region,} \\ \tilde{u}_3(x) & \text{if the solution is not smooth and } \{I_i, I_{i+1}, I_{i+2}\} \text{ is in the smooth region.} \end{cases} \quad (11)$$

To implement a specific solution technique, we extended the principle of the central WENO interpolation defined in [8].

First, we construct an ENO interpolant as a convex combination of polynomials that are based on different discrete stencils.

Specifically, we define in the discrete cell  $I_i$ :

$$\tilde{u}^i(x) \equiv \sum_j w_j \times \tilde{u}_j(x), \quad \sum_j w_j = 1, w_j \geq 0 \quad j \in \{1, 2, 3, c\}, \quad (12)$$

$\tilde{u}_1(x)$ ,  $\tilde{u}_2(x)$  and  $\tilde{u}_3(x)$  are the previously defined polynomials.  $\tilde{u}_c(x)$  is the second-order polynomial defined on the central stencil  $\{I_{i-2}, I_{i-1}, I_i, I_{i+1}, I_{i+2}\}$ .

$\tilde{u}_c(x)$  is calculated such that the convex combination (12), will be fifth-order accurate in smooth regions.

Therefore, it must verify:

$$\tilde{u}_{\text{opt}}(x) = \sum_j C_j \times \tilde{u}_j(x) \quad \forall x \in I_i, \quad \sum_j C_j = 1, \quad C_j \geq 0, \quad j \in \{1, 2, 3, c\}. \quad (13)$$

The constants  $C_j$  represent ideal weights for (12). As already noted in [8], the freedom in selecting these constants has no influence on the properties of the numerical stencil; any symmetric choice in (13), provides the desired accuracy for  $\tilde{u}_{\text{opt}}(x)$ .

In what follows, we make the choice:  $C_1 = C_3 = 1/8$ ,  $C_2 = 1/4$ ,  $C_c = 1/2$ . Then the central polynomial,  $\tilde{u}_c(x)$ , can be calculated from (13):

$$\tilde{u}_c(x) = [\tilde{u}_{\text{opt}}(x) - C_1 \tilde{u}_1(x) - C_2 \tilde{u}_2(x) - C_3 \tilde{u}_3(x)] / C_c \quad \forall x \in I_i. \quad (14)$$

Note that, although the stencil defining  $\tilde{u}_c(x)$  is the five-points stencil  $\{I_{i-2}, I_{i-1}, I_i, I_{i+1}, I_{i+2}\}$ , this polynomial is only a second-order approximation of  $u(x)$ . This is not a drawback since the role of  $\tilde{u}_c(x)$  is only to recover high-order of accuracy in smooth regions.

To complete the reconstruction of  $\tilde{u}^i(x)$  and to ensure properties (11), it is left to compute the non-oscillatory weights,  $w_j$ . To define these weights, we follow the reasoning of [2].

To achieve the optimal interpolation, (13), in smooth regions, the weights  $w_j$  must smoothly converge to the ideal weights  $C_j$  as  $\Delta x$  approaches zero. In an opposite way, in regions where a discontinuity does exist, the weights should effectively remove the contribution of stencils that contain the discontinuity, according to properties (11).

To this end, combining (12) and (13) gives

$$\tilde{u}^i(x) = \tilde{u}_{\text{opt}}(x) + \sum_{j \in \{1, 2, 3, c\}} (w_j - C_j) \times \tilde{u}_j(x) \quad \forall x \in I_i. \quad (15)$$

Since  $\tilde{u}_j(x) = u(x) + O(\Delta x^3)$ ,  $j \in \{1, 2, 3, c\}$ , wherever the solution is smooth (15) can be re-written as

$$\tilde{u}^i(x) = \tilde{u}_{\text{opt}}(x) + \sum_{j \in \{1, 2, 3, c\}} (w_j - C_j) \times (u(x) + O(\Delta x^3)) \quad \forall x \in I_i. \quad (16)$$

Therefore, the second term of (16) must be at least a  $O(\Delta x^5)$  quantity for  $u(x)$  to be approximated at fifth-order by  $\tilde{u}^i(x)$  in regions of smoothness.

Then the necessary and sufficient conditions are

$$\begin{cases} \left( \sum_{j \in \{1,2,3,c\}} w_j - 1 \right) \times u(x) = O(\Delta x^5), \\ \sum_{j \in \{1,2,3,c\}} (w_j - C_j) = O(\Delta x^2). \end{cases} \quad (17)$$

It is sufficient to require

$$\begin{cases} \sum_{j \in \{1,2,3,c\}} w_j - 1 \leq O(\Delta x^5), \\ w_j - C_j \leq O(\Delta x^2), \quad w_j \geq 0 \quad \forall j \in \{1, 2, 3, c\}. \end{cases} \quad (18)$$

Up to this point, the development of the fifth-order WENO scheme has been general. To fully determine the CWENO5 scheme, we need now to specify the non-oscillatory weights.

#### 2.4. The non-oscillatory weights

To begin, we calculate the general indicators of smoothness defined in [2]:

$$IS_j^i \equiv \frac{1}{u_{\max}^2} \sum_k \Delta x_i^{2k-1} \times \int_{I_i} \left( \frac{d^k \tilde{u}_j}{dx^k} \right)^2 dx, \quad j \in \{1, 2, 3, c\}, \quad (19)$$

where  $u_{\max}$  is calculated over the whole calculation domain  $\Omega$ :  $u_{\max} = \max_{x \in \Omega} |u|$ . These indicators provide a measure of the smoothness of the solution over the cell  $I_i$ , according to the particular stencil selected to define  $\tilde{u}_j(x)$  on that cell.

In regions of smoothness,  $IS_j^i \ll 1$ , whereas  $IS_j^i = O(1)$  in cells with strong gradients or discontinuities.

Specifically, formula (19) can be explicitized for  $\tilde{u}_1(x)$ ,  $\tilde{u}_2(x)$  and  $\tilde{u}_3(x)$  ( $\equiv \sum_{j=1}^3 a_{j-1} x^{j-1}$ ) on a non-uniform mesh:

$$IS_j^i = a_1^2 \Delta x_i^2 + \frac{13}{3} a_2^2 \Delta x_i^4 + O(\Delta x_i^6), \quad j \in \{1, 2, 3\}. \quad (20)$$

For  $\tilde{u}_c(x)$ , formula (19) and definition (14) give

$$IS_c^i = a_1^2 \Delta x_i^2 + \left( \frac{13}{3} a_2^2 + \frac{1}{2} a_1 a_3 \right) \Delta x_i^4 + O(\Delta x_i^6). \quad (21)$$

For each quadratic polynomial ( $\tilde{u}_j(x)$ ,  $j \in \{1, 2, 3\}$ ), the polynomial coefficients  $\{a_p\}$  are calculated by numerically inverting (4). The coefficients for  $\tilde{u}_c(x)$  are then deduced from formula (14). When the mesh is uniform, the coefficients  $\{a_p\}$  are explicitly given by formulae (6), (8), (9) and (10). The polynomial coefficients for  $\tilde{u}_c(x)$  are then determined.

The general form of  $IS_j^i$  is then

$$IS_j^i = a_1^2 \Delta x_i^2 (1 + O(\Delta x_i^2)). \quad (22)$$

If the  $j$ th stencil lies in smooth monotone regions, then  $a_1 = O(1)$  and consequently,  $IS_j^i = O(\Delta x_i^2) \ll 1$ . If a discontinuity appears in the  $j$ th stencil, then  $a_1 = O(1/\Delta x_i)$  and  $IS_j^i = O(1)$ .

Hence, having calculated  $IS_j^i$ , we can now define the non-oscillatory weights,  $w_j$ , that verify conditions (18).

According to [2], these weights are defined by

$$w_j \equiv \frac{\alpha_j}{\sum_{p \in \{1,2,3,c\}} \alpha_p}, \quad j \in \{1, 2, 3, c\} \quad (23)$$

with

$$\alpha_p \equiv \frac{C_p}{(\varepsilon(u) + IS_p^i)^2}, \quad p \in \{1, 2, 3, c\}, \quad (24)$$



where we introduced the following modification in (24):  $\varepsilon(u)$  is a function which measures the regularity of the solution,  $u$ , in the entirety of the computational domain,  $\Omega$ . This function is defined to correct – at least theoretically – some deficiencies that may appear in some cases if one uses the procedure defined in [2].

To simply illustrate this point, let us suppose that the optimum five-points stencil,  $\{I_{i-2}, I_{i-1}, I_i, I_{i+1}, I_{i+2}\}$ , lies in the regions of smoothness of the solution.

Then, the classical procedure gives us the following result:

$$\alpha_p \equiv \frac{C_p}{(\varepsilon + O(\Delta x_i^2))^2}, \quad p \in \{1, 2, 3, c\}, \quad (25)$$

where  $\varepsilon$  is defined as a “positive real number which is introduced to avoid the denominator to become zero” [2]. Usually, this parameter is taken equal to  $1 \times 10^{-6}$ , independent of the solution. However, as already noted in [6] or [7],  $\varepsilon$  is a dimensional quantity and should not only be only selected so as to prevent an indeterminate form of (25).

Indeed, on relatively coarse meshes, it may happen that the term  $O(\Delta x_i^2)$  in (25) be greater than  $\varepsilon$  (let us note that, numerically, the term  $O(\Delta x_i^2)$  in (25) has no reasons to have exactly the same value from one stencil to another). The consequence is that the non-oscillatory weights,  $w_p$ , verify the following property:

$$w_p = O(1) > 0, \quad \sum_p w_p = 1, \quad p \in \{1, 2, 3, c\}. \quad (26)$$

Although this result ensures that all the non-oscillatory weights are different from zero (i.e all the polynomials are conserved in (12)), it does not verify the second condition in (18). This means that the numerical scheme is only third-order accurate, in such a case.

To remedy this, there exist two solutions.

First, one can select a finer mesh such that the denominator of (25) is predominated by  $\varepsilon$  (term  $O(\Delta x_i^2)$  lower than  $\varepsilon$ ). In such a case, we obtain the expected result,  $w_p = C_p + O(\Delta x_i^2)$ , and the scheme becomes fifth-order accurate. This way, we may obtain a “super convergence” phenomenon that sometimes appears in some computations.

But, necessarily, a question arises: what is the utility of a high-order method if one is condemned to use fine meshes to get the advantages of an optimum theoretical accuracy?

The solution to palliate this difficulty – this is the second solution – is to take into account the dimensional meaning of  $\varepsilon$  by selecting  $\varepsilon \equiv O(1)$  in (25). Indeed, with such a choice we obtain again the “ad-hoc result”:  $w_p = C_p + O(\Delta x_i^2)$ ; however, this result now remains valid even if the mesh is coarse.

The function we introduced into (24) tries to mimic this latter solution to preserve the convergence properties of the scheme, even on coarse meshes.

This function is defined as follows:

$$\varepsilon(u) \equiv \left[ \frac{\min_{p \in \{1, 2, 3, c\}} (\overline{IS}_p)}{\max_i \{ \max_{p \in \{1, 2, 3, c\}} (IS_p^i) \}} \right]^2. \quad (27)$$

With  $\overline{IS}_p \equiv \|IS_p^i\|_{L_1} \quad \forall p \in \{1, 2, 3, c\}$ .

The value of  $\varepsilon(u)$  is actualized at each time-step and constitutes a global measurement of the regularity of the solution in  $\Omega$ ; unfortunately, a local definition of  $\varepsilon(u)$  did not give successful results on numerical tests.

Now, the WENO scheme using this new function has the following properties.

If the solution is smooth over the domain  $\Omega$ , then  $\varepsilon(u) = O(1)$  since both the numerator and denominator of (27) are  $O(\Delta x_i^2)$ . In such a case, the coefficient  $\alpha_p$ , verifies the property:

$$\alpha_p = \frac{C_p}{(O(1) + O(\Delta x_i^2))^2}. \quad (28)$$

Consequently, we have for the non-oscillatory weights,  $w_p$ :

$$w_p = C_p + O(\Delta x_i^2), \quad p \in \{1, 2, 3, c\}. \quad (29)$$



This result, combined with the definition, (23), ensures that the sufficient conditions, (18), are satisfied: the resulting scheme is therefore fifth-order accurate in the smooth regions, whatever the mesh considered.

Now, if there exists a discontinuity in the five-points stencil,  $\{I_{i-2}, I_{i-1}, I_i, I_{i+1}, I_{i+2}\}$ , one or more of the  $p(p \in \{1, 2, 3, c\})$  candidate stencils reside in smooth regions of the numerical solution. In such a case,  $\varepsilon(u) = O(\Delta x_i^4)$  because  $\min_i \{\min_p (IS_p)\} = O(\Delta x_i^2)$  and  $\max_i \{\max_p (IS_p^i)\} = O(1)$ . Then, for stencils that lie in the smooth region:

$$\alpha_p = \frac{C_p}{(O(\Delta x_i^4) + O(\Delta x_i^2))^2} \Rightarrow w_p = O(1) + O(\Delta x_i^2). \quad (30)$$

In this case, the non-oscillatory weights,  $w_p$ , do not resemble the ideal weights anymore: the scheme becomes third order accurate. If the  $p$ th stencil is smooth, then the  $p$ th polynomial defined from this stencil is useful and should be utilized. The result above verifies this principle and definition (23) ensures the convexity of the combination of these polynomials: the resulting scheme remains monotone.

Lastly, for non-smooth reduced stencils included into the optimum stencil, we have the following property:

$$\alpha_p = \frac{C_p}{(O(\Delta x_i^4) + O(1))^2} \Rightarrow w_p = O(\Delta x_i^4). \quad (31)$$

Therefore, for small  $\Delta x_i$ , the weight assigned to the non-smooth stencil vanishes as  $\Delta x_i \rightarrow 0$ .

Thus, we designed, at the theoretical level up to now, a modified WENO procedure that ensures the ENO properties of the interpolation in the regions of discontinuities while preserving the optimal properties of convergence when the solution is smooth.

## 2.5. The CWENO5 scheme for scalar hyperbolic problems

The final form of the CWENO5 scheme is given by

$$\left. \frac{\partial f}{\partial x} \right|_i = \frac{(\tilde{f}_{i+1/2} - \tilde{f}_{i-1/2})}{\Delta x_i} \quad (32)$$

and

$$\tilde{u}_{i+1/2}^L = \sum_{j \in \{1, 2, 3, c\}} w_j \times \tilde{u}_j(x_{i+1/2}), \quad (33)$$

$\tilde{f}_{i+1/2}$  is calculated by the Roe's method (formula (2)). The non-oscillatory weights,  $\{w_j\}$ , are given by (23) and calculated from (20), (21), (24) and (27).

When the grid is uniform, the computations are simplified by using formulae (6), (8) and (9) for the polynomial coefficients.

Then, the calculation of  $(\tilde{u}_{i+1/2}^L, \tilde{u}_{i-1/2}^R)$  produces the following simplified result:

$$\begin{cases} \tilde{u}_{i-1/2}^R = \left(-\frac{7}{120}w_c - \frac{1}{6}w_1\right)\bar{u}_{i-2} + \left(\frac{1}{3}w_2 + \frac{5}{6}w_1 + \frac{21}{40}w_c\right)\bar{u}_{i-1} \\ \quad + \left(\frac{5}{6}w_2 + \frac{1}{3}w_1 + \frac{11}{6}w_3 + \frac{73}{120}w_c\right)\bar{u}_i + \left(-\frac{1}{6}w_2 - \frac{7}{6}w_3 - \frac{7}{120}w_c\right)\bar{u}_{i+1} + \left(\frac{1}{3}w_3 - \frac{1}{60}w_c\right)\bar{u}_{i+2}, \\ \tilde{u}_{i+1/2}^L = \left(-\frac{1}{60}w_c + \frac{1}{3}w_1\right)\bar{u}_{i-2} + \left(-\frac{1}{6}w_2 - \frac{7}{6}w_1 - \frac{7}{120}w_c\right)\bar{u}_{i-1} \\ \quad + \left(\frac{5}{6}w_2 + \frac{1}{3}w_3 + \frac{11}{6}w_1 + \frac{73}{120}w_c\right)\bar{u}_i + \left(\frac{1}{3}w_2 + \frac{5}{6}w_3 + \frac{21}{40}w_c\right)\bar{u}_{i+1} + \left(-\frac{1}{6}w_3 - \frac{7}{120}w_c\right)\bar{u}_{i+2}. \end{cases} \quad (34)$$

## 2.6. Extension to non-linear systems: the one-dimensional Euler equations

In this section, we extend the CWENO5 scheme to solve systems of hyperbolic conservation laws. Specifically, we consider the one-dimensional Euler equations in the following conservation form:

$$\frac{\partial \mathbf{U}}{\partial t} + \frac{\partial \mathbf{F}(\mathbf{U})}{\partial x} = 0, \quad (35)$$

where

$$\mathbf{U} \equiv [\rho, \rho u, \rho E]^t, \quad \mathbf{F} \equiv [\rho u, \rho u^2 + p, \rho u H]^t \quad (36)$$

$H \equiv E + p/\rho$  is the specific total enthalpy and this set of equations is closed by the equation-of-state of an ideal gas:  $p = (\gamma - 1)(\rho E - u^2/2)$ ,  $\gamma = 1.40$ .

As in the scalar case, the semi-discrete conservative finite-volume scheme discretizing (35) is written as

$$\frac{d\bar{U}_i}{dt} = -\frac{1}{\Delta x_i} [\tilde{F}_{i+1/2} - \tilde{F}_{i-1/2}]. \quad (37)$$

Instead of using the Roe's method to calculate  $\tilde{\mathbf{F}}_{i+1/2}$ , we selected the HLL (Harten, Lax and Van-Leer) approximate Riemann solver [9]. Indeed, the HLL solver is one of the simplest shock-capturing schemes, as it does not require the knowledge of the eigenvectors of (35). Therefore, such a solver is easier to implement for solving (35). As an extra bonus, this scheme is not subject to numerical problems such as odd–even decoupling in propagating shocks, problems that one can encounter using Roe's scheme, for example.

Thus, in this approach, the numerical flux  $\tilde{\mathbf{F}}_{i+1/2}$  is calculated according to the following formula:

$$\tilde{F}_{i+1/2} = \frac{\lambda_{i+1/2}^+ F(U_{i+1/2}^L) - \lambda_{i+1/2}^- F(U_{i+1/2}^R)}{\lambda_{i+1/2}^+ - \lambda_{i+1/2}^-} + \frac{\lambda_{i+1/2}^+ \times \lambda_{i+1/2}^-}{\lambda_{i+1/2}^+ - \lambda_{i+1/2}^-} \times (U_{i+1/2}^R - U_{i+1/2}^L). \quad (38)$$

The characteristic velocities of the scheme are given by

$$\begin{cases} \lambda_{i+1/2}^+ \equiv \max(u_{i+1/2}^L + a_{i+1/2}^L, u_{i+1/2}^R + a_{i+1/2}^R, 0), \\ \lambda_{i+1/2}^- \equiv \min(u_{i+1/2}^L - a_{i+1/2}^L, u_{i+1/2}^R - a_{i+1/2}^R, 0). \end{cases} \quad (39)$$

The conservative point-values,  $(\mathbf{U}_{i+1/2}^{L,R})$ , are calculated from the interpolated primitive variables  $[\rho_{i+1/2}^{L,R}, u_{i+1/2}^{L,R}, p_{i+1/2}^{L,R}]^t$ . These variables are interpolated by using the CWENO5 procedure developed in the scalar case. Although this choice is not referenced in the literature as the best one for dealing with one-dimensional problems (a characteristic-wise reconstruction would be more suitable), it has the advantage of being general since its extension to multi-dimensional problems is straightforward. Alternatively, the characteristic variables are undefined for a multi-dimensional hyperbolic problem because the physically relevant characteristic directions are a priori unknown.

Lastly, only one smoothness indicator is calculated for the all the variables of the problem; this indicator is based upon the density,  $\rho$ , since this quantity detects both a shock and a contact discontinuity.

We ensure the time-integration of (37) by using the third-order TVD Runge–Kutta procedure previously mentioned.

### 3. Numerical validation

#### 3.1. Asymptotic stability analysis

First, we study the asymptotic stability of the CWENO5 scheme. To this end, we compute the complex eigenvalues of the matrices obtained by the spatial discretization of the following scalar linear system:

$$\begin{cases} u_t + u_x = -\frac{1}{S} \frac{dS}{dx} u & \forall x \in [-1, 1], \\ u(x = -1, t) = f(t). \end{cases} \quad (40)$$

The computational domain is divided into  $N$  non-uniform intervals of width  $\Delta x_i (\equiv x_{i+1/2} - x_{i-1/2})$ . The spatial derivatives at all grid points, including the boundary points, are discretized by using the algebraic formulae previously developed.

The source term:  $-\frac{1}{S} \frac{dS}{dx} u$ , is introduced to model problems with a varying geometry according to  $x$  (for example, the one-dimensional nozzle flow problem).

In our example, the shape of the geometry is given by  $S(x) \equiv x^2 - x + 1/2$ .

Thus, we write the upwind approximation

$$u_x|_i \approx \frac{u_{i+1/2}^L - u_{i-1/2}^L}{\Delta x_i}. \quad (41)$$

Substituting approximation (41) into the linear problem (40) with the non-periodic boundary conditions at  $x = -1$  leads to a system of ODEs that can be written

$$\frac{d\mathbf{U}}{dt} = \mathbf{M}\mathbf{U} + \mathbf{Q}_u f(t) + \mathbf{S}\mathbf{U}, \quad (42)$$

where  $\mathbf{U} \equiv [\bar{u}_i]^T$  is an  $N$ -dimensional vector representing the values of the solution at the discrete points.

$\mathbf{M}$  is an  $N \times N$  matrix that contains the algebraic coefficients for the discretization and  $\mathbf{S}$  the  $N \times N$  matrix accounting for the source terms. Lastly,  $\mathbf{Q}_u$  is a vector of dimension  $N$  accounting for the boundary conditions at  $x = -1$ .

The asymptotic stability condition for the semi-discrete system (42) is that all eigenvalues of matrix  $\mathbf{M} + \mathbf{S}$  only contain negative real parts. This is a necessary but not sufficient condition for the stability of long-time integration of the system [10].

To begin, we study the spatial discretization of (40) with  $\mathbf{S} \equiv 0$  (no source terms). Fig. 2 gives numerical results for  $N = 100$  and  $N = 200$  grid points and for two grid stretching typified by  $\Delta x_{\min}/\Delta x_{\max} = 1$  (uniform grid) and  $\Delta x_{\min}/\Delta x_{\max} = 0.1$  (stretched grid). As one can see, the discretization is stable and is free of the grid stretching: in the worst case, Fig. 2(b) ( $N = 100$ ,  $\Delta x_{\min}/\Delta x_{\max} = 0.1$ ), the eigenvalue which is closest to the unstable area is such that  $\text{Re}_{\max}(\lambda) = -15.5$ ,  $\text{Im}(\lambda) = -20$ . Consequently, whatever the stretching of the grid or the mesh resolution, the spatial discretization remains stable, Fig. 2(a)–(d). This is still true when a source

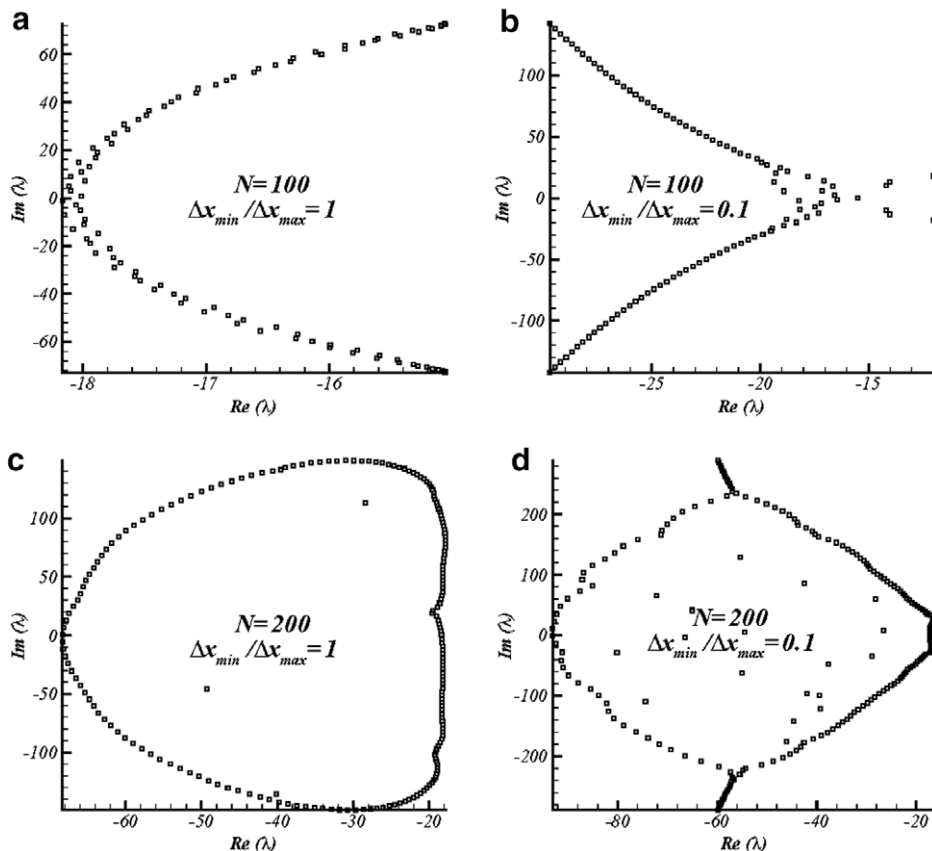


Fig. 2. CWENO5 scheme. Asymptotic stability analysis: eigenvalue spectra for the discretization of  $u_x$ . Influence of grid stretching,  $\Delta x_{\min}/\Delta x_{\max}$  and grid resolution,  $N$ .

term is introduced in the scalar equation. Indeed, the real part of the discrete eigenvalues is strictly negative everywhere, Fig. 3.

However, one can note that the stability region is slightly reduced ( $\text{Re}_{\max}(\lambda) \approx -4$ ) for the case  $N = 100$ ,  $\Delta x_{\min}/\Delta x_{\max} = 0.1$ , Fig. 3(b).

Now, we study the time-integration of (42) by the third-order Runge–Kutta TVD procedure [15]. For these computations, the CFL is selected such that  $\Delta t/\min_i(\Delta x_i) = 0.8$ . To be stable, the temporal integration of (42) must be such that the values of the complex factor of amplification, remain in the area defined by the unit circle centred at the origin [10]. First, Fig. 4 presents numerical results with no source terms ( $S \equiv 0$  in (42)). As one can see, the CWENO5 scheme with Dirichlet boundary conditions is stable even on stretched meshes, Fig. 4(b), since the discrete eigenvalue spectrum lies in the stability area. Now, if we introduce a source term in (42), we get the results presented in Fig. 5. We can see that the scheme remains stable, even if the mesh is stretched ( $N = 200$ ,  $\Delta x_{\min}/\Delta x_{\max} = 0.1$ ), Fig. 5(b).

To conclude the first study, one can say that the discretization of (40) by the optimum fifth-order interpolation is free of the grid stretching even if there exists a source term. In addition, the influence of the boundary conditions does not seem to impose a heavy constraint on the CFL number. Practically, the maximum CFL number allowed by the stability constraint is found to be equal to 1.55 if  $\Delta x_{\min}/\Delta x_{\max} = 1$  and to 1.59 if  $\Delta x_{\min}/\Delta x_{\max} = 0.1$ .

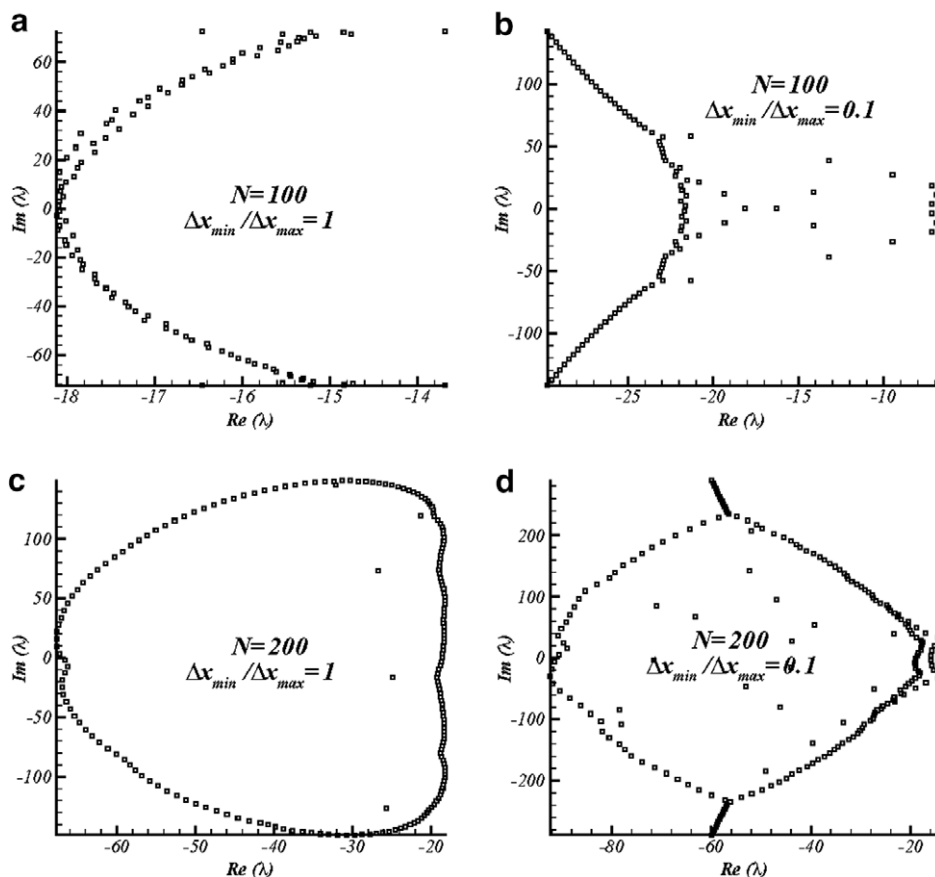


Fig. 3. CWENO5 scheme. Asymptotic stability analysis: eigenvalue spectra for the discretization of  $u_x + \frac{1}{S} \frac{dS}{dx} u$ . Influence of the mesh resolution,  $N$ , for a given stretching of the grid,  $\Delta x_{\min}/\Delta x_{\max}$ .

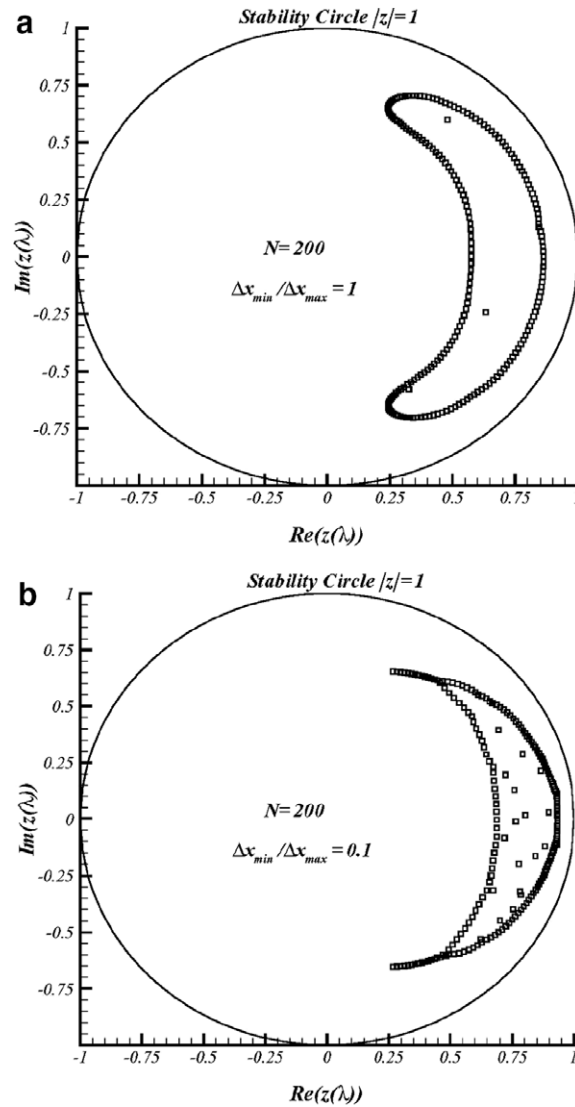


Fig. 4. CWENO5 scheme. Space–time discretization of  $u_t + u_x = 0$ . (a)  $N = 200$ ,  $\Delta x_{min}/\Delta x_{max} = 1$ , CFL = 0.8 (b)  $N = 200$ ,  $\Delta x_{min}/\Delta x_{max} = 0.1$ , CFL = 0.8.

### 3.2. Simulation of shock-induced sound

To simulate such a problem, we use the linear problem proposed by Casper and Carpenter [11].

We consider the scalar problem:

$$u_t + a(x)u_x = 0, \quad u(x, 0) = \begin{cases} 1/2, & x < x_s, \\ 1, & x > x_s, \end{cases} \quad a(x) = \begin{cases} 2, & x < x_s, \\ 1, & x > x_s, \end{cases} \quad \forall x \in [0, 1]. \quad (43)$$

The inflow boundary condition is  $u(0, t) = \frac{1}{2}(1 + \delta \times \sin \omega t)$ .

This problem models the interaction of a sound wave with a shock. The ability to obtain an accurate solution to such problem is important in the development of shock-capturing methods for CAA research, for example.

Practically, we made the following choices:  $\delta = 10^{-5}$ ,  $\omega = 16\pi$ ,  $x_s = 1/2$ . Computations are run up to  $t = 1.25$  (10 temporal periods of the initial signal).

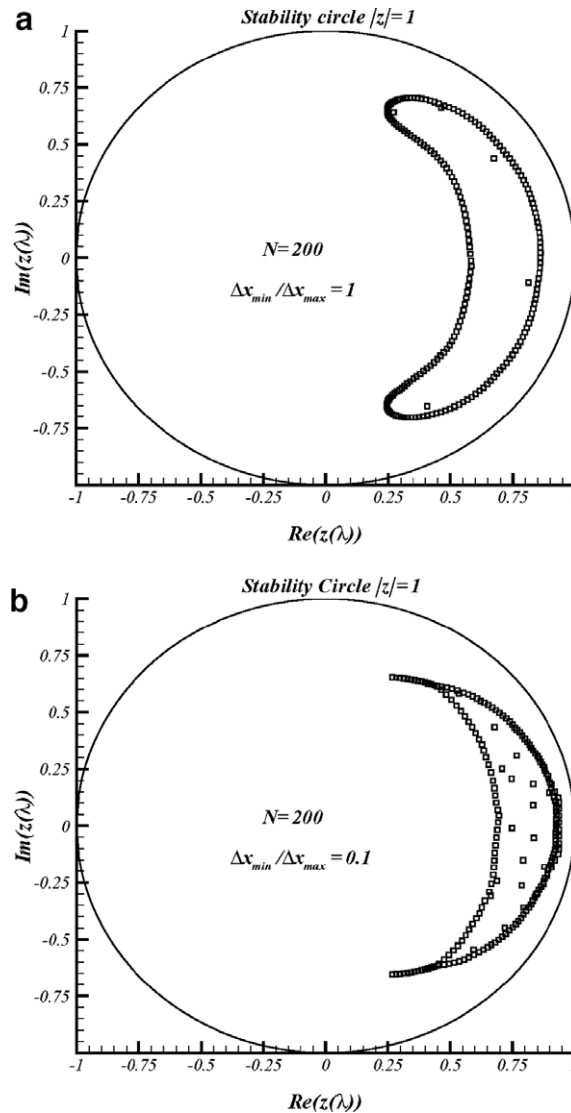


Fig. 5. CWENO5 scheme. Space–time discretization of  $u_t + u_x = -\frac{1}{5} \frac{dS}{dt} u$  (a)  $N = 200$ ,  $\Delta x_{min}/\Delta x_{max} = 1$ , CFL = 0.8 (b)  $N = 200$ ,  $\Delta x_{min}/\Delta x_{max} = 0.1$ , CFL = 0.8.

First, this problem is discretized by the CWENO5 scheme. For all the computations, we selected a CFL ( $\equiv \max_i a(x_i) \Delta t / \Delta x$ ) number equal to 0.5. To compare with a competing finite-volume method, we chose a uniform mesh ( $\Delta x_i \equiv \Delta x$ ). The competing method selected is the “classical” fifth-order WENO scheme (WENO5 scheme) of Shu [2], ( $\varepsilon = 10^{-6}$  in the calculation of the non-oscillatory weights).

To begin, Fig. 6(a) presents numerical results for the CWENO5 scheme, for  $N = 160$  grid points. As one can see it, the structure of the sound wave is preserved after having crossed the shock wave. To compare with the UWENO5 scheme of Shu, we consider Fig. 6(b). These results are comparable with the precedents.

Then, Fig. 7 compares the numerical errors of both schemes: once again, the results are equivalent for both schemes. The corresponding non-oscillatory weights,  $w_j$ , are plotted in the computational domain for the CWENO5 scheme, Fig. 8(a). These results are obtained with definition (27) for  $\varepsilon$ : as one can note it, except at the two grid points defining the shock, the weights  $w_j$  reach their ideal values everywhere ( $w_1 = w_3 = 0.125$ ,  $w_2 = .25$ ). However, exactly the same results are obtained if one uses the “classical” value

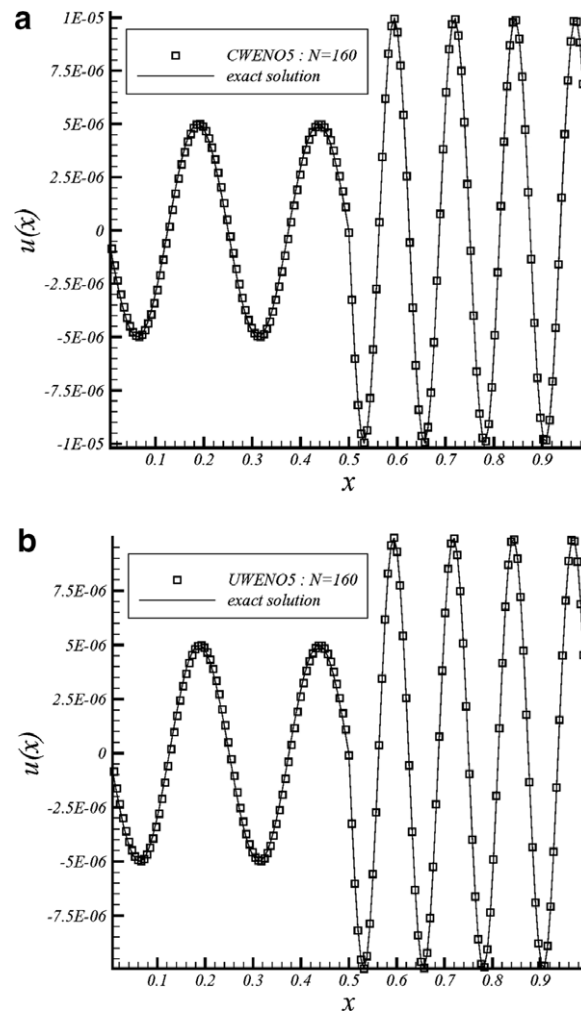


Fig. 6. Simulation of shock-induced sound. CWENO5 scheme. Linear problem  $u_t + a(x)u_x = 0$ ,  $u(0, t) = \frac{1}{2}(1 + \varepsilon \sin \omega t)$ .  $N = 160$ ,  $\text{CFL} = 0.5$ ,  $t = 1.25$ ,  $\varepsilon = 10^{-5}$ ,  $\omega = 16\pi$ .

for  $\varepsilon$  ( $\varepsilon = 10^{-6}$ ): this means that the new way of calculating  $\varepsilon$  by (27) does not bring anything in this case. This result is confirmed if one considers the numerical error of discretization for both solutions in the computational domain, Fig. 8(b).

At this point, therefore, one may conclude that the CWENO5 scheme is equivalent to the “classical” UWENO5 scheme.

### 3.3. Non-linear scalar problem: the Burgers equation

We solve the following non-linear scalar Burgers equation:

$$u_t + \left( \frac{u^2}{2} \right)_x = 0 \quad \forall x \in [0, 2] \quad (44)$$

with the initial condition:  $u(x, t = 0) = 1/2 + \sin(\pi x)$  and a 2-periodic boundary condition. Generally speaking, the CFL number is defined as  $\max_i |u_i^n| \Delta t / \min_i \Delta x_i$ . Its value is taken as 0.5 for both CWENO5 and UWENO5 schemes except for the accuracy tests where a low CFL number ( $\text{CFL} = 0.01$ ) is selected to



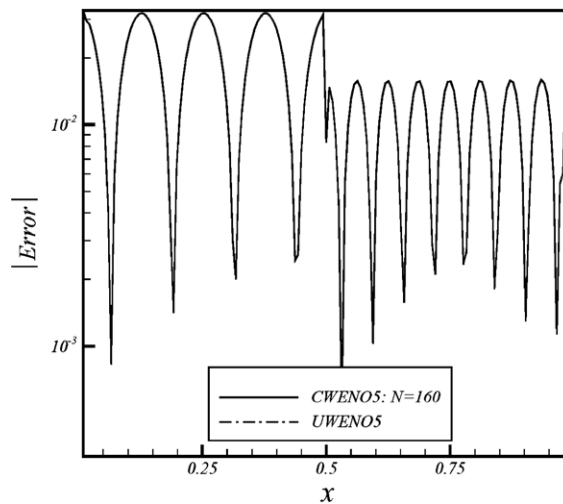


Fig. 7. Simulation of shock-induced sound: linear problem  $u_t + a(x)u_x = 0$ . Comparison of the numerical errors in the computational domain between the CWENO5 scheme and the UWENO5 scheme ( $N = 160$  grid points).

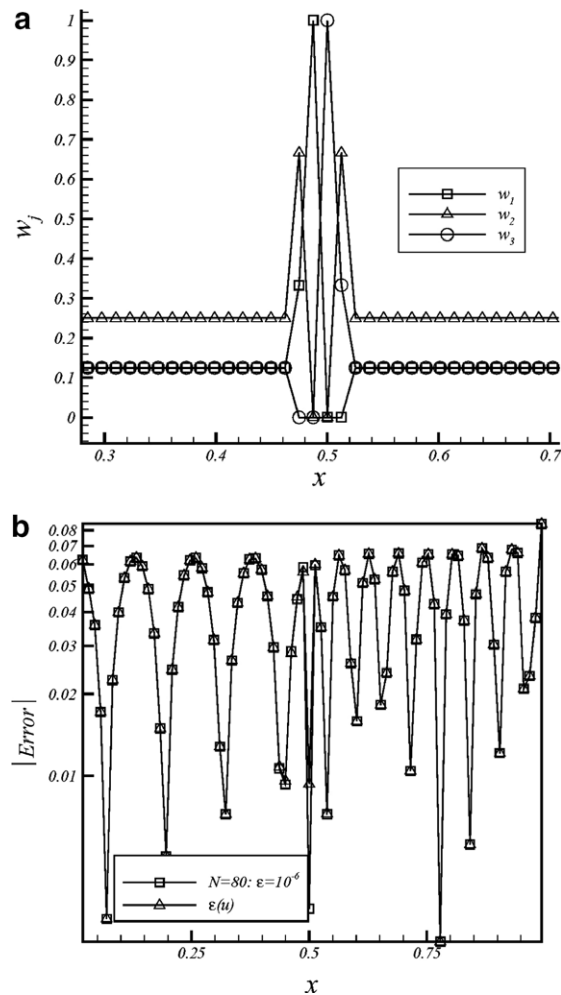


Fig. 8. CWENO5 scheme. Simulation of shock-induced sound: linear problem  $u_t + a(x)u_x = 0$ . (a) Non-oscillatory weights ( $N = 80$ ), (b) Discretization error for  $\varepsilon \equiv 10^{-6}$  and  $\varepsilon \equiv \varepsilon(u)$ .

guarantee that spatial error dominates. To begin, a uniform mesh ( $\Delta x_i \equiv \Delta x$ ) with  $N$  cells is used for this test case.

When  $t = 1/2\pi$ , the solution is still smooth and the discrete errors and numerical orders of accuracy are shown in Table 1 (CWENO5 scheme,  $\varepsilon = 10^{-6}$ ) and Table 2 (CWENO5 scheme,  $\varepsilon \equiv \varepsilon(u)$  given by (27)). As can be seen, both versions reach their designed order of accuracy; however, the solution with  $\varepsilon \equiv \varepsilon(u)$  produces a lower error level on the same mesh. In addition, the convergence towards the theoretical order of accuracy is more regular with this latter solution. Fig. 9 explains this result: we compare the non-oscillatory weights for the classical solution ( $\varepsilon = 10^{-6}$ ) and the new solution ( $\varepsilon \equiv \varepsilon(u)$ ), for a relatively coarse mesh ( $N = 40$  grid points). We can see that the non-oscillatory weights have their ideal values almost everywhere for the new solution; this is no more the case if one considers the solution with  $\varepsilon = 10^{-6}$ : one then encounters the drawback we noticed in the previous section and the method loses its high accuracy on coarse meshes. Of course, when the mesh is refined, the non-oscillatory weights obtained for  $\varepsilon = 10^{-6}$  reach their ideal values. However, it is proved that formula (27) brings a substantial improvement in accuracy on coarse meshes, as long as the solution remains smooth. To complete this analysis, Table 3 presents the numerical results obtained with the UWENO5 scheme: the results are very similar with those obtained with the CWENO5 scheme for  $\varepsilon = 10^{-6}$ .

When  $t = 3/2\pi$ , a shock has already appeared in the solution and it is located at  $x = 1.238$ .

To begin, Fig. 10 shows the non-oscillatory weights for both solutions:  $\varepsilon = 10^{-6}$  (Fig. 10(a)) and  $\varepsilon \equiv \varepsilon(u)$  (Fig. 10(b)). As one can see it, both results are similar; as already noticed in the preceding test case, the new procedure (27) does not bring any advantage in regions where a discontinuity appears. The results that follow are obtained with formula (27).

Thus, Fig. 11 shows the numerical solution on two meshes: a uniform mesh with  $N = 80$  grid points (Fig. 11(a)) and a stretched mesh near the shock place ( $\Delta x_{\min}/\Delta x_{\max} = 0.1$ ) (Fig. 11(b)). As one can note it, the shock is captured without any numerical oscillation in both cases and its resolution is improved when the mesh is stretched. In Fig. 12(a), we compare the CWENO5 scheme with the UWENO5 scheme on a uniform mesh: in both cases, the shock is captured in the same way though these schemes are structurally very different. Fig. 12(b) confirms this fact: the discretization errors in the computational domain for both schemes can be regarded as equivalent.

Table 1

$u_t + uu_x = 0$ ;  $u(x, t = 0) = 1/2 + \sin(\pi \times x)$ ; CWENO5 scheme with periodic boundary conditions;  $t = 1/2\pi$ ; CFL = 0.010;  $\varepsilon = 10^{-6}$ .  $L_1$  and  $L_\infty$  errors

$N$	$L_1$ error	$L_1$ order	$L_\infty$ error	$L_\infty$ order
10	$9.30 \times 10^{-3}$	–	$1.25 \times 10^{-2}$	–
20	$1.44 \times 10^{-3}$	2.7	$3.80 \times 10^{-3}$	1.7
40	$1.06 \times 10^{-4}$	3.7	$2.59 \times 10^{-4}$	3.8
80	$4.73 \times 10^{-6}$	4.5	$2.36 \times 10^{-5}$	3.4
160	$1.58 \times 10^{-7}$	4.9	$1.27 \times 10^{-6}$	4.5
320	$3.05 \times 10^{-9}$	5.7	$1.51 \times 10^{-8}$	6.3

Table 2

$u_t + uu_x = 0$ ;  $u(x, t = 0) = 1/2 + \sin(\pi \times x)$ ; CWENO5 scheme with periodic boundary conditions;  $t = 1/2\pi$ ; CFL = 0.010;  $\varepsilon \equiv \varepsilon(u)$ .  $L_1$  and  $L_\infty$  errors

$N$	$L_1$ error	$L_1$ order	$L_\infty$ error	$L_\infty$ order
10	$5.10 \times 10^{-3}$	–	$1.06 \times 10^{-2}$	–
20	$6.88 \times 10^{-4}$	2.9	$3.05 \times 10^{-3}$	1.8
40	$4.05 \times 10^{-5}$	4.1	$2.10 \times 10^{-4}$	3.9
80	$1.38 \times 10^{-6}$	4.8	$1.04 \times 10^{-5}$	4.3
160	$4.75 \times 10^{-8}$	4.9	$3.60 \times 10^{-7}$	4.8
320	$1.52 \times 10^{-9}$	5	$1.18 \times 10^{-8}$	4.9

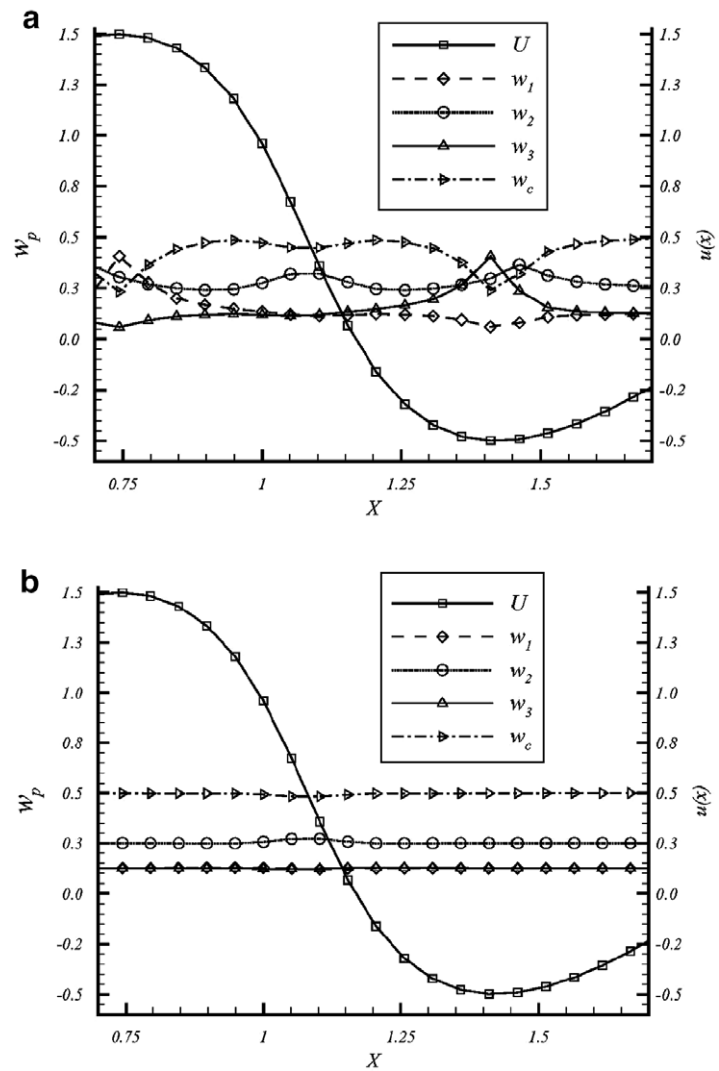


Fig. 9. CWENO5 scheme. Burgers equation. Case without shock.  $u(x, t = 0) = 1/2 + \sin(\pi x)$ ,  $t = 1/2\pi$ ,  $N = 40$ ,  $CFL = 0.01$ . Non-oscillatory weights: (a)  $\varepsilon \equiv 10^{-6}$ , (b)  $\varepsilon \equiv \varepsilon(u)$ .

Table 3  
 $u_t + uu_x = 0$ ;  $u(x, t = 0) = 1/2 + \sin(\pi \times x)$ ; UWENO5 scheme with periodic boundary conditions;  $t = 1/2\pi$ ;  $CFL = 0.010$ ;  $\varepsilon = 10^{-6}$ .  $L_1$  and  $L_\infty$  errors

$N$	$L_1$ error	$L_1$ order	$L_\infty$ error	$L_\infty$ order
10	$9.52 \times 10^{-3}$	–	$1.71 \times 10^{-2}$	–
20	$1.41 \times 10^{-3}$	2.7	$3.26 \times 10^{-3}$	2.4
40	$9.10 \times 10^{-5}$	4	$3.01 \times 10^{-4}$	3.4
80	$3.96 \times 10^{-6}$	4.5	$1.74 \times 10^{-5}$	4.1
160	$1.46 \times 10^{-7}$	4.8	$8.63 \times 10^{-7}$	4.3
320	$3.81 \times 10^{-9}$	5.3	$1.98 \times 10^{-8}$	5.8

3.4. One-dimensional hyperbolic systems: the Euler equations

Unless mentioned, the computations are run on a uniform mesh,  $\Delta x_i \equiv \Delta x$ .  $N$  grid points are utilized to discretize the equations.

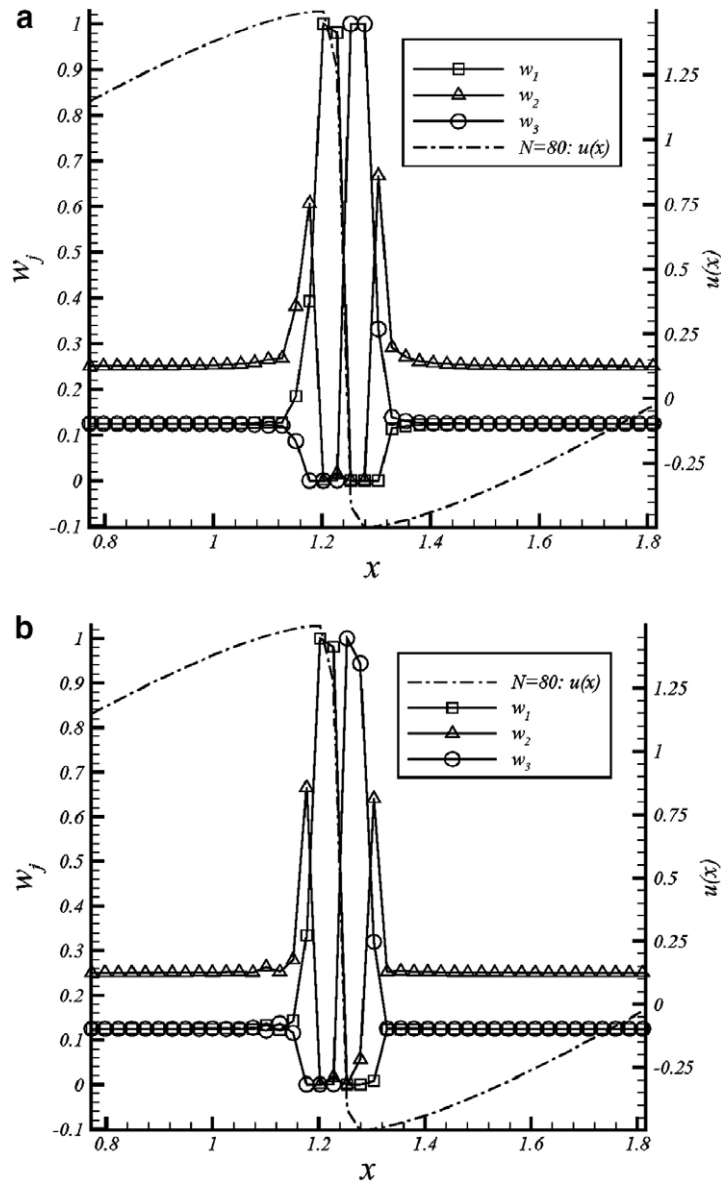


Fig. 10. CWENO5 scheme. Burgers equation. Case with shock.  $u(x, t = 0) = 1/2 + \sin(\pi x)$ ,  $t = 3/2\pi$ ,  $N = 80$ , CFL = 0.50. Non-oscillatory weights: (a)  $\varepsilon \equiv 10^{-6}$ , (b)  $\varepsilon \equiv \varepsilon(u)$ .

The CFL number is defined as

$$\text{CFL} \equiv \Delta t \times \frac{\max_i (|u_i| + a_i)}{\min_i \Delta x_i},$$

where  $a_i \equiv \sqrt{\frac{\gamma p}{\rho}}|_i$  represents the speed of sound for an ideal gas.

We choose CFL = 0.5 for almost all test cases, except for the accuracy tests.

**Example 1.** We solve the Euler equations, (35), in the domain  $[0, 2]$ . The initial condition is set to be  $\rho(x, t = 0) = 1 + 0.2 \times \sin(\pi x)$ ,  $u(x, t = 0) = 1$ ,  $p(x, t = 0) = 1$ , with a 2-periodic boundary condition. The

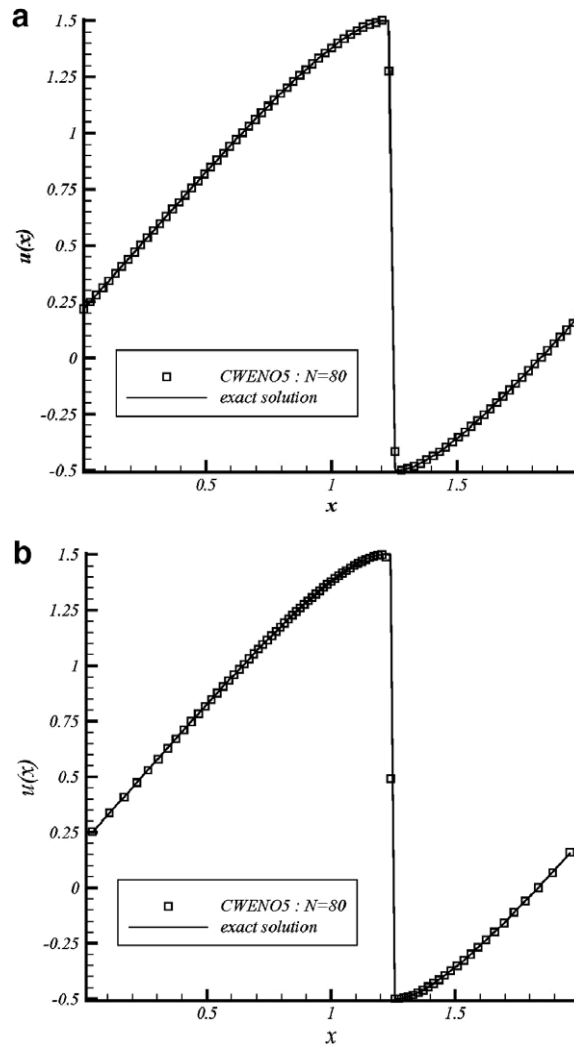


Fig. 11. Burgers equation. Case with shock.  $u(x, t = 0) = 1/2 + \sin(\pi x)$ ,  $t = 3/2\pi$ ,  $N = 80$ ,  $CFL = 0.5$ . CWENO5 scheme: (a) uniform mesh, (b) non-uniform mesh ( $\Delta x_{\min}/\Delta x_{\max} \approx 0.1$ ).

numerical solution is computed up to  $t = 2$  with  $CFL = 0.02$  for both schemes. The errors and numerical orders of accuracy of the density,  $\rho$ , for the CWENO5 scheme (resp. UWENO5 scheme) are shown in Table 4 ( $\varepsilon = 10^{-6}$ ) and Table 5 ( $\varepsilon \equiv \varepsilon(u)$ ) (resp. Table 6). Both schemes have trouble to reach their theoretical order of accuracy when  $\varepsilon = 10^{-6}$  (Tables 4 and 6): this first result agrees with that obtained in the scalar case.

Once again, the CWENO5 scheme with formula (27) remains the most accurate one and presents an almost monotone convergence.

**Example 2 (Sod problem).** This problem and the one that follows only contain shocks and simple smooth region solutions. It is simply used to demonstrate the non-oscillatory properties of the CWENO5 scheme near discontinuities and to validate the specific choices made for the non-oscillatory weights.

The Sod problem is defined by the following left- and right-initial states:

$$(\rho, u, p) = (1, 0, 1) \quad \forall x \leq 0.5, \quad (\rho, u, p) = (0.125, 0, 0.1) \quad \forall x > 0.5.$$

To discretize the computational domain  $[0, 1]$ , we use 200 grid points. The solution is run up to  $t = 0.14$ .

Although this problem is not necessarily a good test for high-order shock capturing schemes (a good second-order ENO scheme would suffice, see [1] for example), we can see that the CWENO5 scheme performs

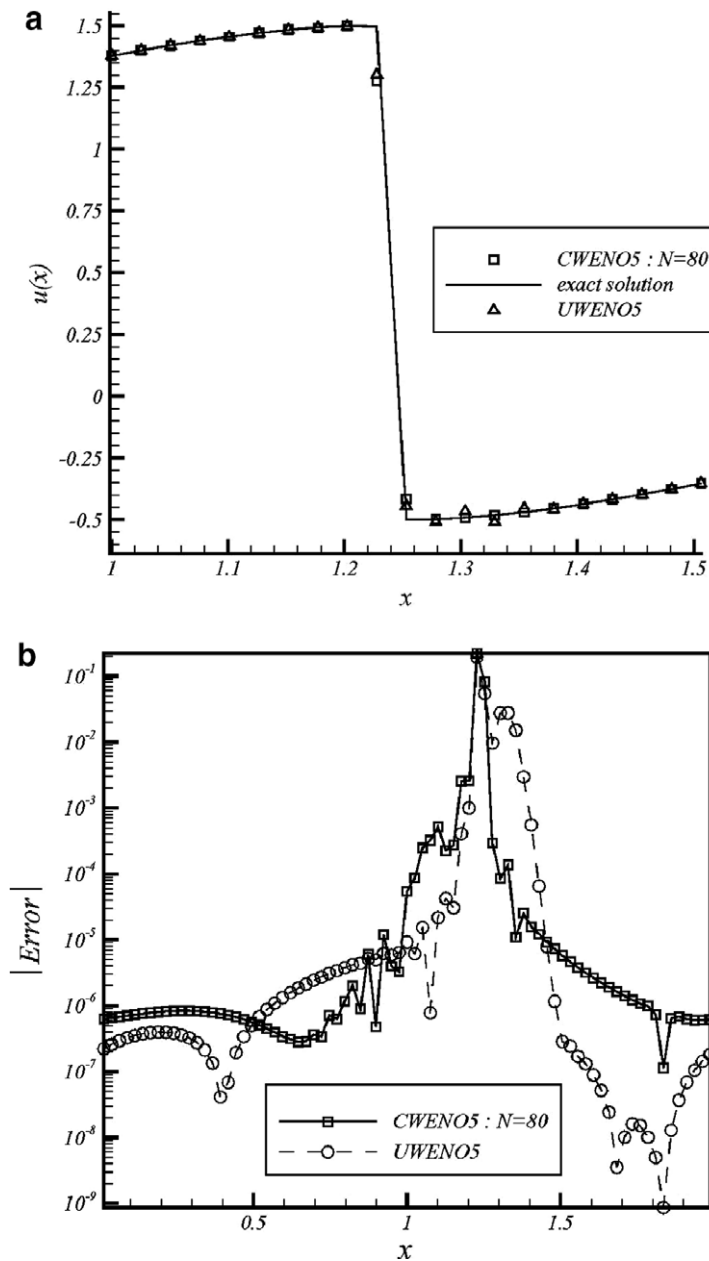


Fig. 12. Burgers equation. Case with shock.  $N = 80$ ,  $t = 3/2\pi$  Comparison between the CWENO5 scheme and the UWENO5 scheme. (a) computed solution, (b) discretization error.

reasonably well, Fig. 13 left. The contact discontinuity is smeared more than the shock, Fig. 13(a) left. In addition, it is interesting to note that the component-wise reconstruction is not as oscillatory as expected; this is no more the case when one considers the UWENO5 scheme, Fig. 13 right. Indeed, noticeable oscillations appear in regions where the solution varies. Of course, these oscillations become less significant when the mesh is refined; however, this result demonstrates the sensitivity of the UWENO5 scheme to the choice of the reconstruction. Better results would be obtained with a characteristic-wise reconstruction [12,19].

**Example 3 (Lax problem).** The Lax problem is defined by the following left- and right-initial states:

$$(\rho, u, p) = (0.445, 0.698, 3.528) \quad \forall x \leq 0, \quad (\rho, u, p) = (0.5, 0, 0.571) \quad \forall x > 0,$$

Table 4

One-dimensional Euler equations  $\rho(x, t=0) = 1 + 0.2 \times \sin(\pi x)$ ,  $u(x, t=0) = 1$ ,  $p(x, t=0) = 1$  CWENO5 scheme with periodic boundary conditions  $t = 2$ ; CFL = 0.020;  $\varepsilon = 10^{-6}$ .  $L_1$  and  $L_\infty$  errors of density  $\rho$

$N$	$L_1$ error	$L_1$ order	$L_\infty$ error	$L_\infty$ order
10	$6.66 \times 10^{-2}$	–	$6.10 \times 10^{-2}$	–
20	$2.05 \times 10^{-3}$	5	$2.13 \times 10^{-3}$	4.8
40	$4.05 \times 10^{-5}$	5.7	$3.41 \times 10^{-5}$	6
80	$8.30 \times 10^{-7}$	5.7	$5.96 \times 10^{-7}$	5.8
160	$1.71 \times 10^{-8}$	5.6	$1.12 \times 10^{-8}$	5.7
320	$4.97 \times 10^{-10}$	5.1	$5.08 \times 10^{-10}$	4.5

Table 5

One-dimensional Euler equations  $\rho(x, t=0) = 1 + 0.2 \times \sin(\pi x)$ ,  $u(x, t=0) = 1$ ,  $p(x, t=0) = 1$  CWENO5 scheme with periodic boundary conditions  $t = 2$ ; CFL = 0.020;  $\varepsilon \equiv \varepsilon(u)$ .  $L_1$  and  $L_\infty$  errors of density  $\rho$

$N$	$L_1$ error	$L_1$ order	$L_\infty$ error	$L_\infty$ order
10	$2.05 \times 10^{-2}$	–	$1.55 \times 10^{-2}$	–
20	$5.15 \times 10^{-4}$	5.2	$4.04 \times 10^{-4}$	5.2
40	$1.44 \times 10^{-5}$	5.2	$1.13 \times 10^{-5}$	5.2
80	$4.24 \times 10^{-7}$	5.1	$3.32 \times 10^{-7}$	5.1
160	$1.30 \times 10^{-8}$	5	$1.01 \times 10^{-8}$	5
320	$4.01 \times 10^{-10}$	5	$3.24 \times 10^{-10}$	5

Table 6

One-dimensional Euler equations  $\rho(x, t=0) = 1 + 0.2 \times \sin(\pi x)$ ,  $u(x, t=0) = 1$ ,  $p(x, t=0) = 1$  UWENO5 scheme with periodic boundary conditions  $t = 2$ ; CFL = 0.020;  $\varepsilon = 10^{-6}$ .  $L_1$  and  $L_\infty$  errors of density  $\rho$

$N$	$L_1$ error	$L_1$ order	$L_\infty$ error	$L_\infty$ order
10	$8.61 \times 10^{-2}$	–	$6.93 \times 10^{-2}$	–
20	$3.42 \times 10^{-3}$	4.7	$2.93 \times 10^{-3}$	4.6
40	$7.70 \times 10^{-5}$	5.4	$6.63 \times 10^{-5}$	5.4
80	$1.40 \times 10^{-6}$	5.8	$1.09 \times 10^{-6}$	6
160	$2.31 \times 10^{-8}$	5.9	$1.60 \times 10^{-8}$	6
320	$5.33 \times 10^{-10}$	5.4	$5.15 \times 10^{-10}$	5

200 grid points are used to discretize the computational domain  $[0, 1]$ . The solution is run up to  $t = 1.30$ . Numerical results are presented in Fig. 14 for the CWENO5 (Fig. 14 left) and the UWENO5 schemes (Fig. 14 right).

Comparing these results to Fig. 13, we see that the component-wise reconstruction here is much “noisier” than in Sod’s problem. The contact discontinuity remains smeared more than the shock but oscillations are clearly visible close to the contact discontinuity, Fig. 14(a). The oscillatory behaviour of the component-wise reconstruction is even more pronounced in the velocity profile, Fig. 14(c). Fortunately, these oscillations become less significant when the mesh is refined. Moreover, these oscillations remain less “noisy” than more classical component-wise reconstructions such as the ENO scheme of Harten et al. [1], or the CWENO scheme of Qiu and Shu [19]. The UWENO5 scheme, Fig. 14 right, remains more oscillatory than the CWENO5 scheme.

Consequently, the CWENO scheme has the important advantage to tolerate component-wise reconstructions, without generating too many significant numerical non-physical oscillations. Moreover, it appears that the single density is a well-adapted sensor for computing the smoothness indicators for all components since the discontinuities remain correctly captured.

**Example 4** (*Interacting blast waves* [20]). We solve the Euler equations, with initial conditions:

$$(\rho, u, p) = \begin{cases} (1, 0, 10^3) & \forall x \in [0, 0.1[, \\ (1, 0, 10^{-2}) & \forall x \in [0.1, 0.9], \\ (1, 0, 10^2) & \forall x \in [0.9, 1]. \end{cases}$$

A reflective boundary condition is applied at both  $x = 0$  and  $x = 1$ .



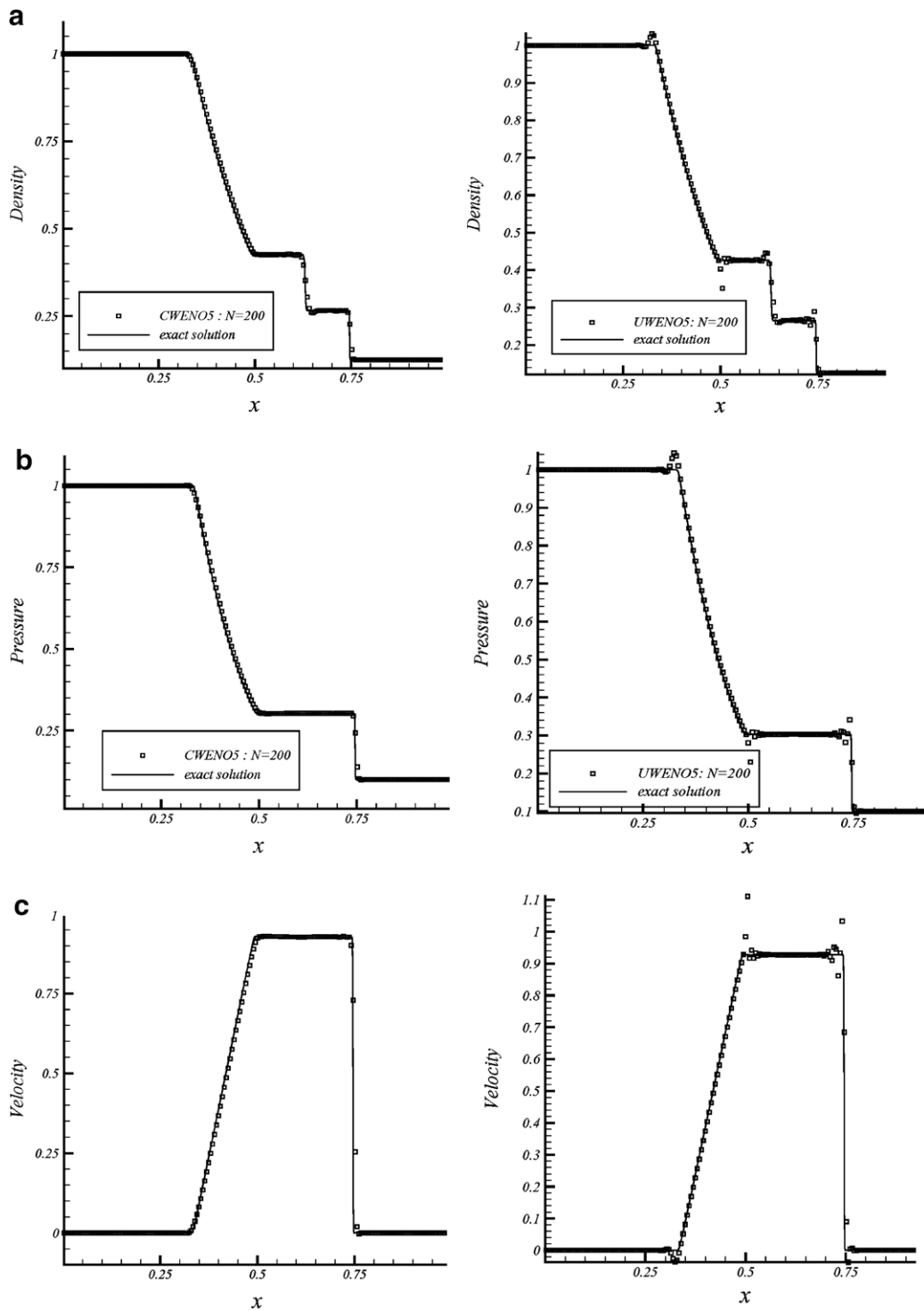


Fig. 13. The Sod problem:  $N = 200$ ,  $t = 0.14$ . (a) density, (b) pressure, (c) velocity Left: CWENO5 scheme. (CFL = 0.5); Right: UWENO5 scheme. (CFL = 0.15).

The computed density  $\rho$  is plotted at  $t = 0.038$  against the “exact” solution; this solution is a converged solution computed by a classical second-order TVD scheme (“minmod” limiter) with 3000 grid points.

In Fig. 15, we show the numerical results of the CWENO5 scheme with  $N = 400$  grid points.

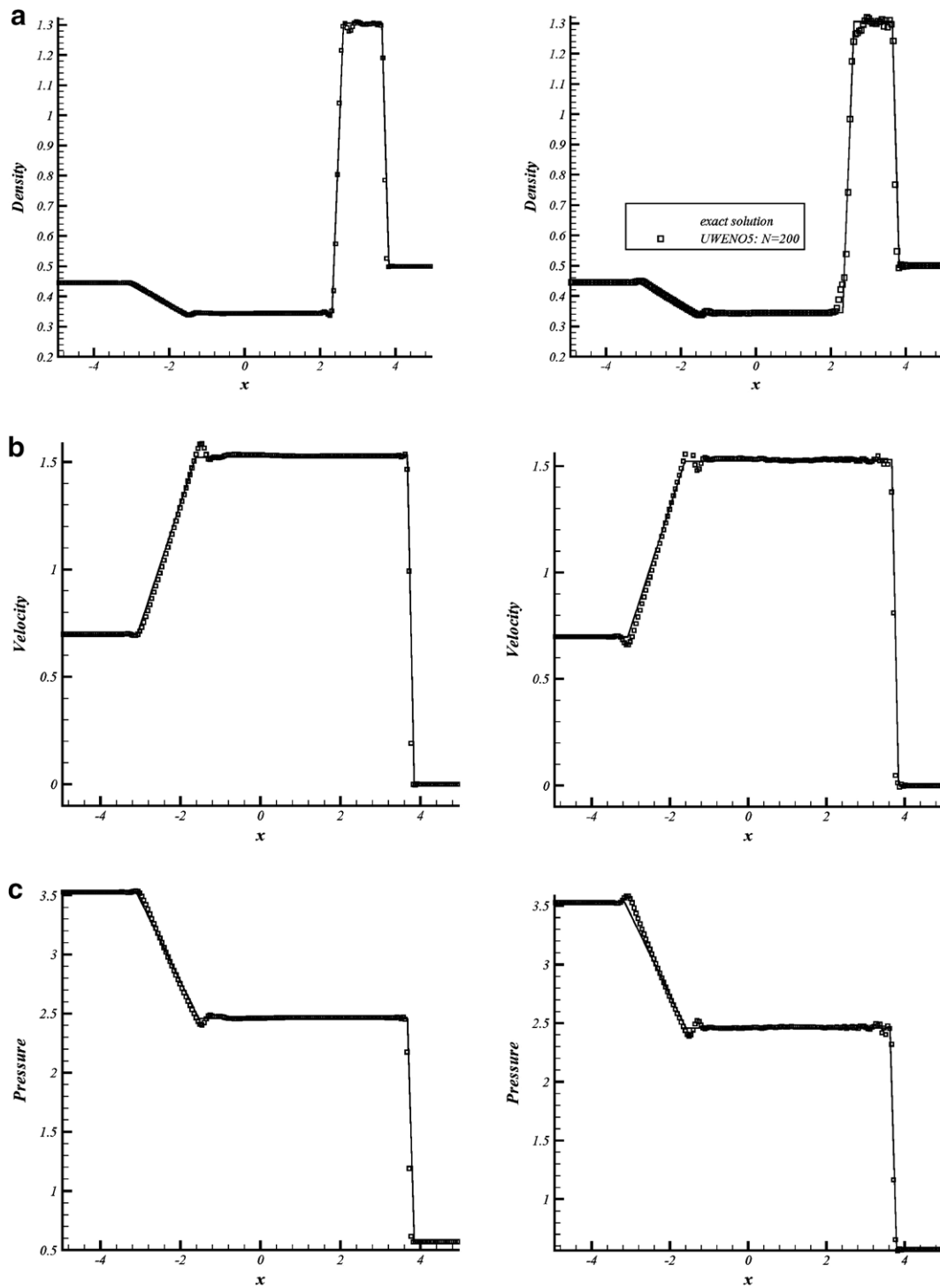


Fig. 14. The Lax problem:  $N = 200$ ,  $t = 1.30$ . (a) density, (b) velocity, (c) pressure. Left: CWENO5 scheme (CFL = 0.5); right: UWENO5 scheme. (CFL = 0.25).

We can see that the three contact waves, near  $x = 0.59$ ,  $0.76$ ,  $0.80$ , are well predicted. In such a case, comparing this solution to the “exact” solution, the CWENO5 scheme resolves the salient features of the flow with a good fidelity and can be considered a “converged” solution.

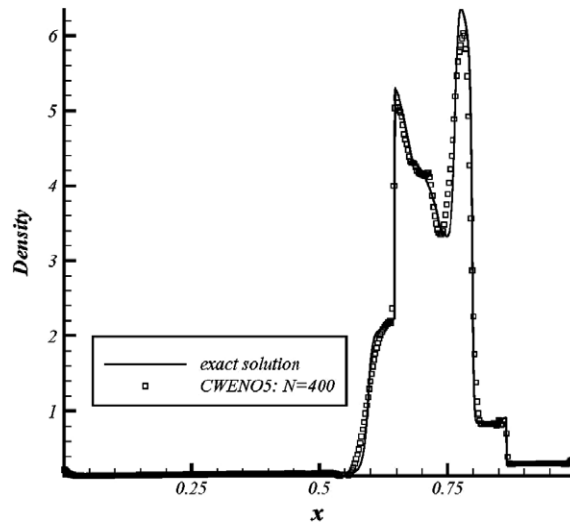


Fig. 15. Blast wave problem. Density  $\rho$ .  $t = 0.038$ ,  $CFL = 0.5$ , CWENO5 scheme:  $N = 400$ .

**Example 5** (*Shock interaction with entropy waves: the Shu–Osher problem* [15]). We solve the Euler equations, (35), with a moving Mach = 3 shock interacting with sine waves in density.

The initial condition is defined as

$$\begin{aligned} (\rho, u, p) &= (3.857143, 2.629369, 10.333333) \quad \forall x < -4, \\ (\rho, u, p) &= (1 + \delta \sin 5x, 0, 1) \quad \forall x \geq -4. \end{aligned}$$

For this test, we take  $\delta = 10^{-2}$ . The computed density  $\rho$  is plotted at  $t = 1.8$  against the “exact” solution; this solution is a converged solution computed by the CWENO5 scheme with 2500 grid points.

In Fig. 16 we show the numerical results of the CWENO5 scheme with  $N = 200$  grid points (Fig. 16(a)) and  $N = 400$  grid points (Fig. 16(b)).

For  $N = 200$ , we can see that the resolution is still insufficient: the amplitude of the entropy waves behind the shock is too much attenuated. This solution is greatly improved with the  $N = 400$  results (Fig. 16(b)): the complex wave patterns after the shock entropy wave interaction are now very well predicted.

**Example 6** (*Shock entropy wave interactions* [2]). This problem is very suitable for high-order shock-capturing schemes because both shocks and complicate smooth flow features co-exist. In this example, a moving shock interacts with an entropy wave of small amplitude.

On the domain  $[0, 5]$ , the initial condition is the following:

$$\begin{aligned} (\rho, u, p) &= (3.857143, 2.629369, 10.333333) \quad \forall x < 1/2, \\ (\rho, u, p) &= (e^{-\delta \sin(kx)}, 0, 1) \quad \forall x \geq 1/2, \end{aligned}$$

where  $\delta$  and  $k$  are the amplitude and the wave number of the entropy wave, respectively.

The mean flow is a right moving Mach 3 shock. If  $\delta$  is small compared to the shock strength, the shock will go to the right of the computational domain, at approximately the non-perturbed shock speed and generate a sound wave that travels along with the flow behind the shock. At the same time, the small amplitude, low-frequency entropy waves are generated in front of the shock. After having interacted with the shock, these waves are compressed in frequency and amplified in amplitude. The main goal of such a test is to check if the structure of the amplified waves is not lost after having crossed the shock wave. Since the entropy wave is very weak relative to the shock, any excessive numerical oscillation could alter the generated waves and the entropy waves.

In our computations, we take  $\delta = 0.01$ . Accordingly, the amplitude of the amplified entropy waves predicted by a linear analysis, [13,14], is 0.08690716 (shown in the following figures as horizontal solid lines).

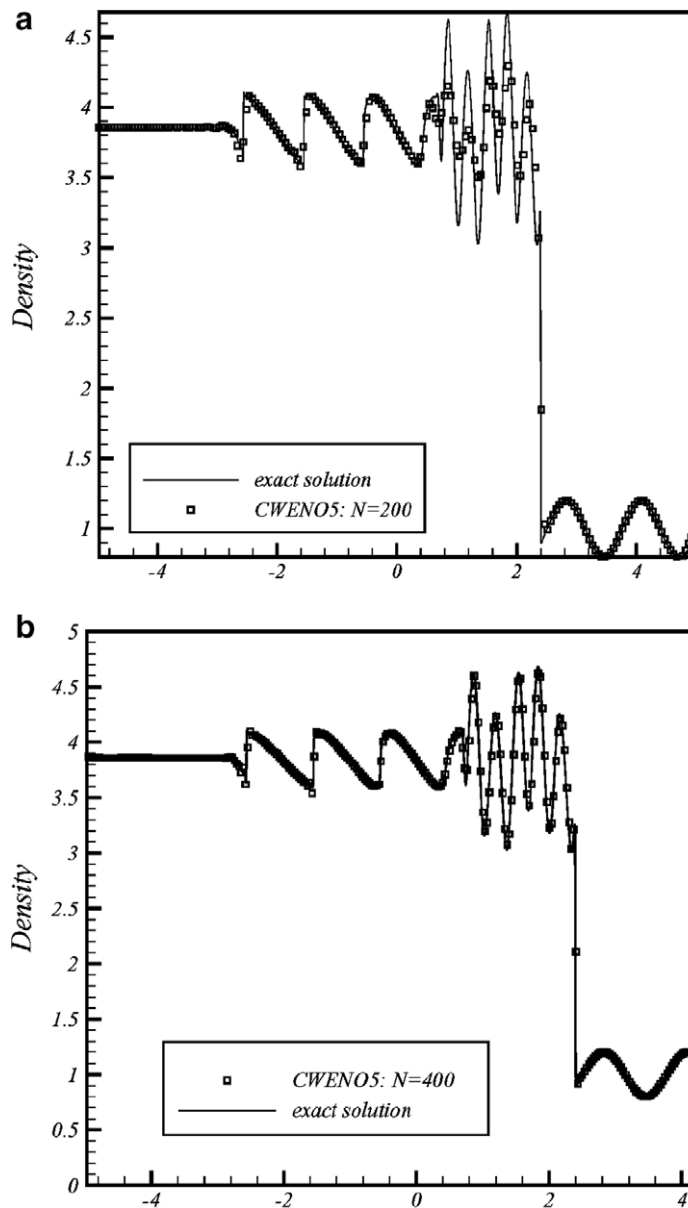


Fig. 16. Shu–Osher problem. Density  $\rho$ .  $t = 1.8$  CWENO5 scheme: (a)  $N = 200$ ,  $\text{CFL} = 0.5$ , (b)  $N = 400$ ,  $\text{CFL} = 0.25$ .

The pre-shock wave number,  $k$ , is selected such that  $k \in \{13, 26\}$ . To get rid of the transient waves due to the initialization, the numerical procedure is defined so that the shock crosses the computational domain three times. The numerical solution is examined when the shock reaches  $x = 4.5$  at  $t = 3.38061$ . For these computations, the CFL is lowered to the value 0.30.

First, for  $k = 13$ , we use 400 grid points, that is effectively 10 points in each wavelength of the generated entropy wave. The results are shown in Fig. 17 (the mean flow has been subtracted from the numerical solution). We can see that on this grid, the CWENO5 scheme calculates the amplified entropy waves quite well, although their amplitude is slightly attenuated, Fig. 17(a). On a grid of 800 points (20 points per wavelength), Fig. 17(b), the resolution becomes very good with the CWENO5 scheme. To compare, we produce the numerical results obtained with 800 grid points, by using the UWENO5 scheme, Fig. 17(c); obviously, this scheme produces equivalent results. Lastly, Fig. 17(d) and (e) produce numerical results for  $k = 26$ ,  $N = 800$  and  $k = 26$ ,

$N = 1200$ , respectively. Even if the amplitude of the entropy waves is slightly attenuated behind the shock, the CWENO5 scheme keeps on giving reasonably good results for 15 points per wavelength, Fig. 17(d).

**Example 7** (*Propagation of sound waves through a transonic nozzle* [16]). The computation of sound propagating through a choked nozzle presents a challenging problem for a shock-capturing scheme. To reduce the complexity of the problem, but retaining the basic physics and difficulties, this propagation problem is modelled by a one-dimensional acoustic wave transmission problem through a transonic nozzle [16].

In this problem, an acoustic wave is introduced at the nozzle inflow region and the sound wave that travels downstream through the transonic nozzle and interacts with the shock is to be calculated. The amplitude of the incoming sound wave is  $\delta = 10^{-5}$ , which is very small compared to the mean values of the flow. The nozzle flow is modelled by the one-dimensional Euler equations with variable nozzle area:

$$\frac{\partial \mathbf{U}}{\partial t} + \frac{\partial \mathbf{F}(\mathbf{U})}{\partial x} = -\frac{1}{A} \frac{dA}{dx} \mathbf{U}', \quad \mathbf{U} \equiv [\rho, \rho u, \rho E]^t, \quad \mathbf{F} \equiv [\rho u, \rho u^2 + p, \rho u H]^t, \quad \mathbf{U}' \equiv [\rho u, \rho u^2, \rho u H]^t. \quad (45)$$

The area of the nozzle is

$$A(x) = \begin{cases} 0.536572 - 0.198086 \times \exp\left(-\text{Log}(2)\left(\frac{x}{0.6}\right)^2\right), & x > 0, \\ 1.0 - 0.661514 \times \exp\left(-\text{Log}(2)\left(\frac{x}{0.6}\right)^2\right), & x < 0. \end{cases}$$

Flow variables are non-dimensionalized by using the upstream values. The velocity scale is  $a_\infty$  (speed of sound), the length scale is  $D$  (diameter of the nozzle) and the density scale is the static density,  $\rho_\infty$ . Then, the mean flow at the inlet is

$$[\bar{\rho}, \bar{u}, \bar{p}]_{\text{inlet}}^t = [1, M_\infty, 1/\gamma]^t. \quad (46)$$

The Mach number at the inlet,  $M_\infty$ , is 0.2006533 and the pressure at the exit,  $p_{\text{exit}}$ , is 0.6071752, so that a shock is formed inside the nozzle. The shock location is then  $x_s = 0.3729$ .

Just upstream of the shock wave, the Mach number is  $M_1 = 1.465$  and downstream,  $M_2 = 0.714$ . The pressure ratio (intensity of the shock wave) is then  $p_2/p_1 = 2.337$ .

The incoming acoustic wave, with angular frequency,  $\omega = 0.6\pi$ , is described as

$$[\rho, u, p]_{\text{acoust}}^t = \delta \times [1, 1, 1]^t \times \sin\left[\omega\left(\frac{x}{1+M_\infty} - t\right)\right]. \quad (47)$$

In the present work, the acoustic wave will be computed directly by solving the non-linear governing equations rather than solving the linearized equations (see [16] for some examples on the linearized problem). This makes it harder to compute the acoustic waves. The challenge is whether the small amplitude wave can still be captured in the computation by the CWENO5 scheme. The computational domain is  $-10 \leq x \leq 10$  and a non-uniform mesh, refined in the throat region, is used.

To begin, the steady state of the nozzle flow is computed. For the flow variables, the initial conditions are specified by using the mean exact solution of this problem. At the boundaries, the back-pressure is specified at the outlet and the total pressure and density are specified at the inlet. The other needed information at both the inlet and outlet are obtained using a first-order extrapolation from their neighbouring mesh points.

The steady-state solution of (45), obtained using a 251 points non-uniform mesh ( $\Delta x_{\min} = 0.10$ ,  $\Delta x_{\max} = 0.49$ ) with CFL = 0.80, is compared with the exact solution, Fig. 18(a). The solution is converged to machine precision, Fig. 18(b). It can be seen that the flow properties are uniform in most regions, of the nozzle, but change dramatically near the nozzle throat, Fig. 18(a). Lastly, the shock is captured without any numerical oscillation. As indicated by the theoretical stability analysis, the stability domain of the CWENO5 is not altered by a strongly varying source-term.

After the steady-state flow-field is computed, the acoustic wave propagation can be simulated using the same non-linear solver. First, the initial conditions are specified using the steady-state solution previously calculated, then, at the inlet, the solution (47) is superimposed for the primitive variables.

Numerical solutions of the acoustic pressure at  $t = 14T$  are shown in Fig. 19 and compared with the analytical solution (given in [16]).

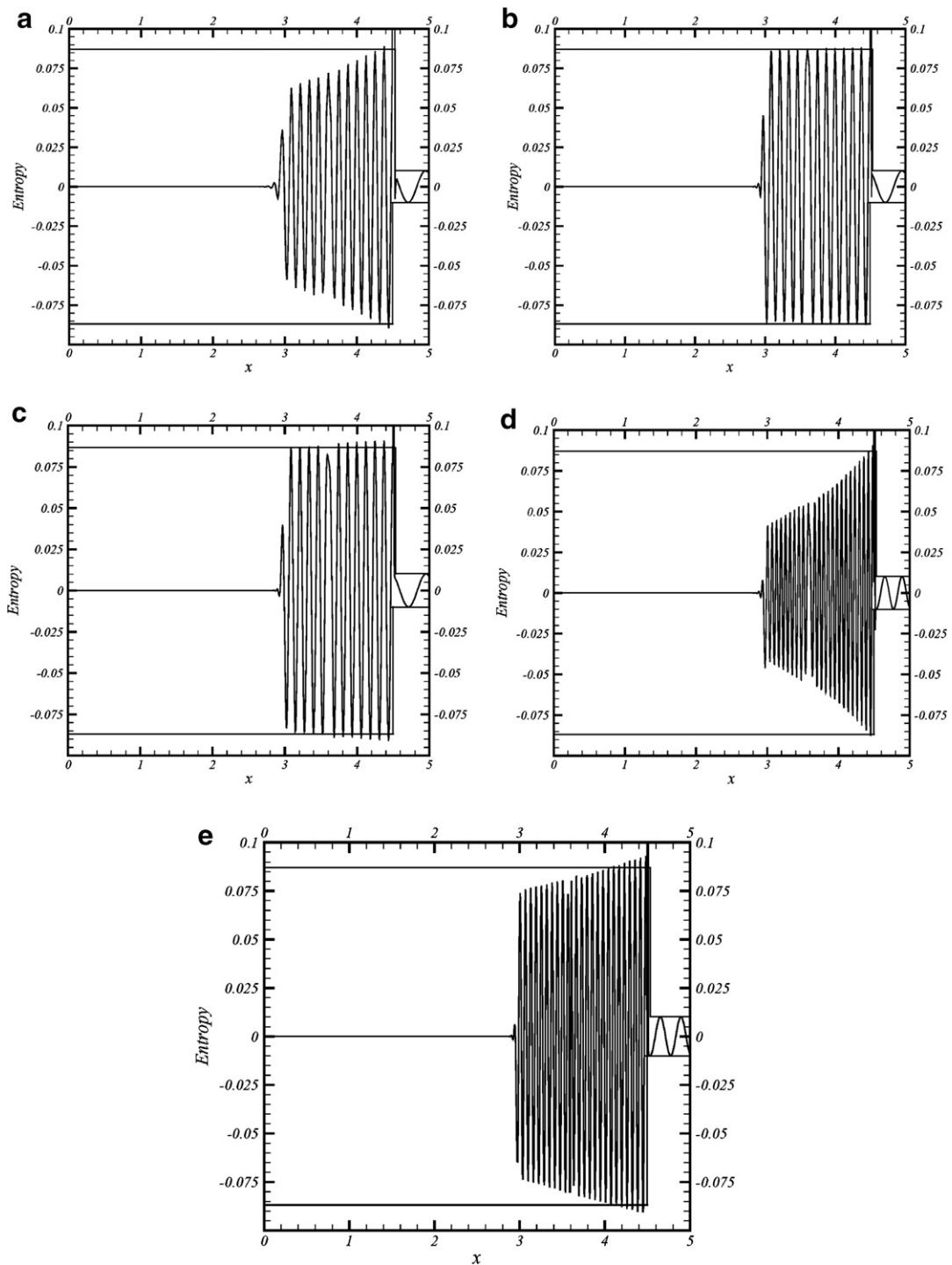


Fig. 17. Shock entropy wave interaction. CWENO5 scheme. CFL = 0.30,  $t = 3.38061$  (a)  $k = 13$ ,  $N = 400$ ; (b)  $k = 13$ ,  $N = 800$ ; (c) UWENO5:  $k = 13$ ,  $N = 800$ ; (d)  $k = 26$ ,  $N = 800$ ; (e)  $k = 26$ ,  $N = 1200$ .

With only 155 grid points, the wave pattern is not correctly captured, Fig. 19(a), while a greatly improved result is produced using a 251 points non-uniform mesh ( $\Delta x_{\min}/\Delta x_{\max} = 0.11$ ), Fig. 19(b). However, the amplitude of the acoustic wave at the shock location is lower than that indicated by the analytical solution:

this is due to the third-order error introduced by the scheme when the WENO procedure modifies the non-oscillatory weights, right at this place.

In spite of this difficulty, one can note that the profiles of the acoustic pressure both upstream and downstream the shock location agree very well with the analytical solution, Fig. 19(b).

### 3.5. The two-dimensional Euler equations

In this section, we illustrate through numerical experiments, the capacity of the CWENO5 algorithm to deal with two-dimensional problems. For this purpose, we discretize the two-dimensional Euler equations for an ideal gas.

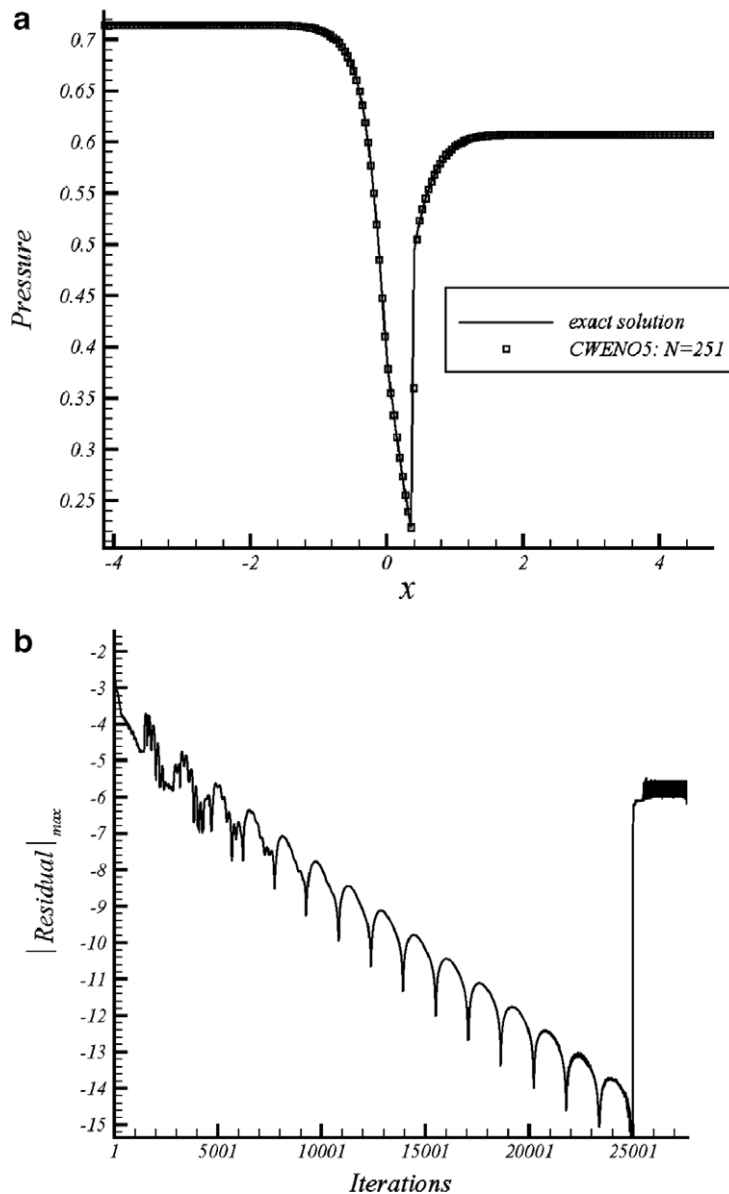


Fig. 18. Propagation of sound waves through a transonic nozzle. Steady-state solution. CWENO5 scheme. Stretched mesh:  $\Delta x_{\min}/\Delta x_{\max} \approx 0.10$  CFL = 0.8,  $N = 251$ . (a) mean pressure, (b) maximum residual.



We use a dimension-by-dimension finite volume approach to extend the algorithm described so far. Doing so, the one-dimensional CWENO5 interpolation, (15), is used in each direction to reconstruct the solution at the cell interfaces. Then, the numerical fluxes are calculated in each direction. The time-integration remains ensured by the TVD RK3 algorithm.

Of course, such an approach neglects the cross-derivatives that necessarily appear in a truly multi-dimensional reconstruction. However, our aim is to demonstrate that, even so, the procedure we developed gives good numerical results for capturing discontinuities that lie oblique to the grid.

To this aim, Riemann problems for two-dimensional gas dynamics are considered, see [18,17,21] for more details on the physics.

To simplify the problem, all the computations are run on a Cartesian mesh in the  $(x,y)$  plane, with  $\Delta x = \Delta y$ .

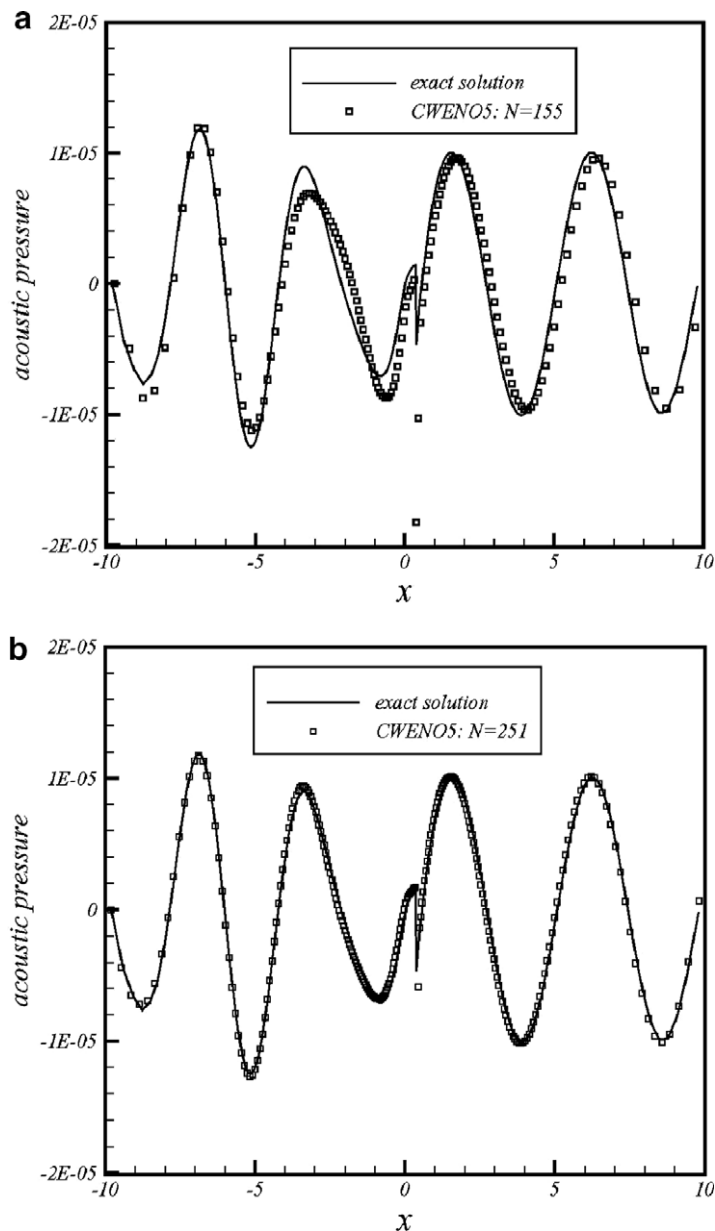


Fig. 19. Propagation of sound waves through a transonic nozzle. Acoustic pressure at  $t = 14T$ . Stretched mesh:  $\Delta x_{\min}/\Delta x_{\max} \approx 0.10$  CWENO5 scheme. CFL = 0.8 (a)  $N = 155$ , (b)  $N = 251$ .

The time-step is now defined as  $\Delta t \equiv \text{CFL} \times \min \left[ \min \left( \frac{\Delta x}{|u|+a} \right), \min \left( \frac{\Delta x}{|v|+a} \right) \right]$ .

**Example 1** (*Radially symmetric Riemann problem* [21]). This test is defined to check the conservation of radial symmetry. For this problem, the initial conditions for the Euler equations are set as follows:

$$(\rho, u, v, p)'(x, y, t = 0) = \begin{cases} (2, 0, 0, 15) & \text{if } \|\vec{x}\| \leq 0.13, \\ (1, 0, 0, 1) & \text{otherwise.} \end{cases}$$

Computations are run up to  $t = 0.13$  on a  $80 \times 80$  rectangular grid. The Courant number is set to 0.75. As a reference solution, a highly resolved solution is computed on a  $400 \times 400$  rectangular mesh. In addition, a second-order TVD scheme, defined by the “Superbee” limiter, is used to check the influence of the reconstruction.

Fig. 20(a) shows contour plots of the density at  $t = 0.13$ . In addition, Figs. 20(b) and (c) show 1D cuts along the  $y = 0.5$  and  $y = x$  lines, compared with the “exact” solution. From these results, the solution appears to be isotropic, Fig. 20(b), and the radius of curvature of the shock at angles not aligned with grid lines is uniform, Fig. 20(a). Moreover, one can note the absence of oscillations behind the shock-wave.

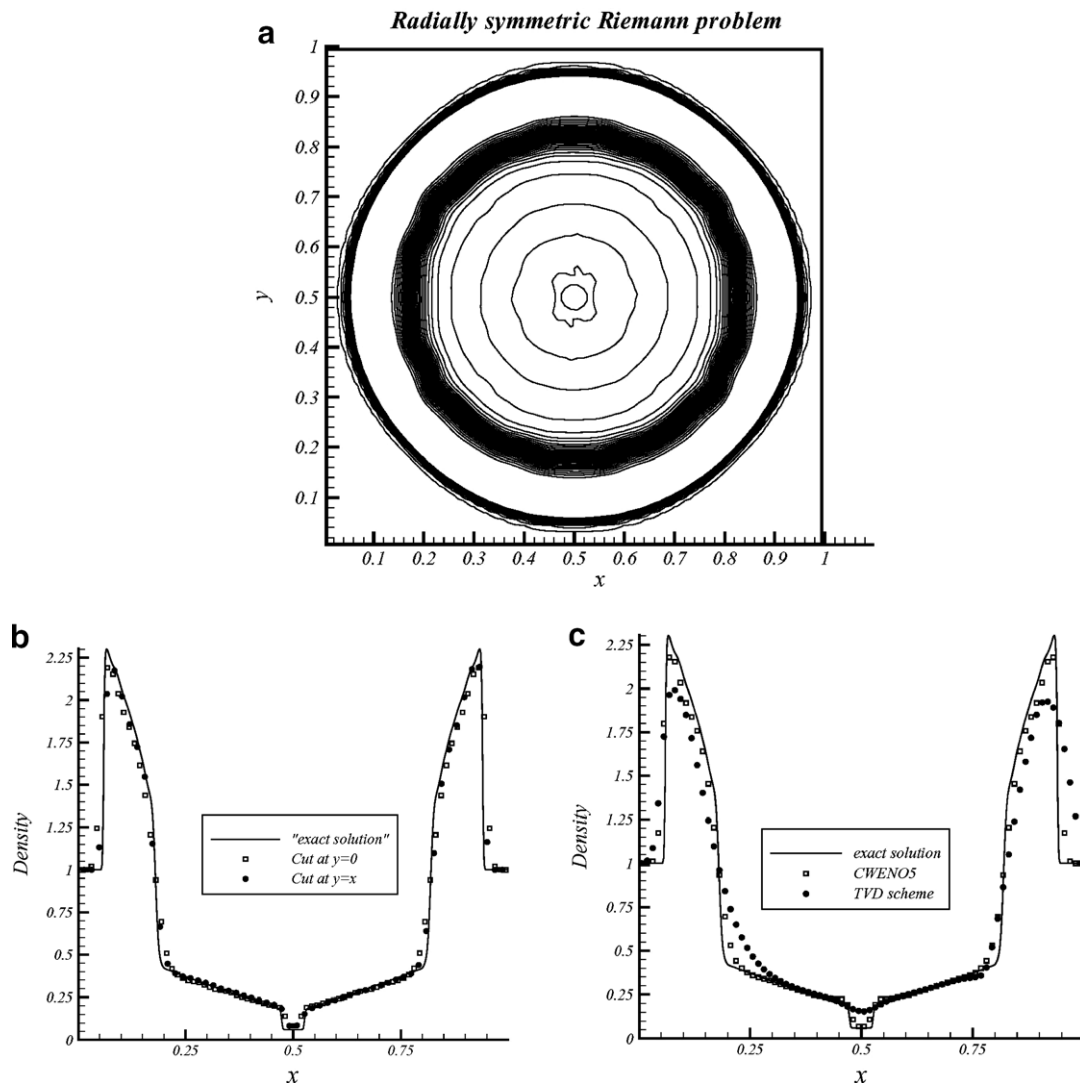


Fig. 20. Two-dimension Euler equations. Radially symmetric Riemann problem.  $80 \times 80$  rectangular grid,  $\text{CFL} = 0.75$ ,  $t = 0.13$ , (a) Density plot, (b) Cuts at  $y = 0$  and  $y = 0.5$ , (c) Comparisons between the CWENO5 and TVD schemes along  $y = 0$ .

Lastly, Fig. 20(c) gives a comparison between the CWENO5 reconstruction and a formally second-order TVD reconstruction obtained with the “Superbee” limiter: one can then appreciate the advantage of using the CWENO5 reconstruction.

**Example 2** (*Two-dimensional Riemann problem* [17,18]). In the  $(x,y)$  plane, we consider the following Riemann problem for the Euler equations:

$$(\rho, u, v, p)'(x, y, t = 0) = (\rho_i, u_i, v_i, p_i)', \quad i \in \{1, 2, 3, 4\}, \quad (48)$$

where  $i$  denotes the  $i$ th quadrant.

According to [18], there exist 15 genuinely different admissible configurations for polytropic gas, separated by the three types of 1D centered waves, namely, rarefaction, shock and contact waves. In this example, we compute some of these configurations. Consult [17,18] for more details.

All the computations are performed on a uniform Cartesian grid consisting of  $400 \times 400$  points. The contour levels are selected as in [17] to compare the results. The CFL number used is 0.75. Lastly, we

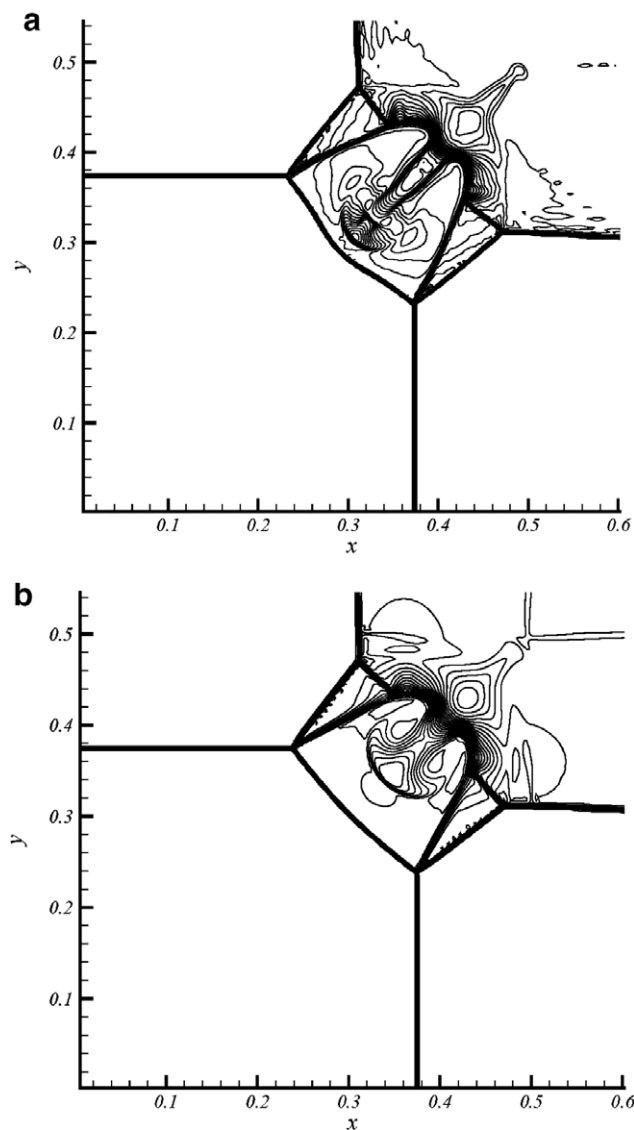


Fig. 21. Two-dimension Euler equations. 2-D Riemann problem. Configuration 3.  $400 \times 400$  rectangular grid,  $\text{CFL} = 0.75$ ,  $t = 0.3$ . Density contour lines (32 contour lines: 0.16–1.71 step 0.05) (a) CWENO5 scheme, (b) “Superbee” limiter.

compare the CWENO5 reconstruction with the second-order TVD scheme used in the preceding example.

Our numerical examples below show the density contour lines subject to four initial data configurations and we refer the reader to [17] for a detailed discussion on the wave formation in each of these configurations.

*Configuration 3:* interaction of four shock waves.

The initial conditions for the 2D Riemann problem (48) are as follows:

$$(\rho, u, v, p)^t = \begin{cases} (1.5, 0, 0, 1.5)^t & \text{if } x > 0, y > 0, \\ (0.5323, 1.206, 0, 0.3)^t & \text{if } x < 0, y > 0, \\ (0.138, 1.206, 1.206, 0.029)^t & \text{if } x < 0, y < 0, \\ (0.5323, 0, 1.206, 0.3)^t & \text{if } x > 0, y < 0. \end{cases}$$

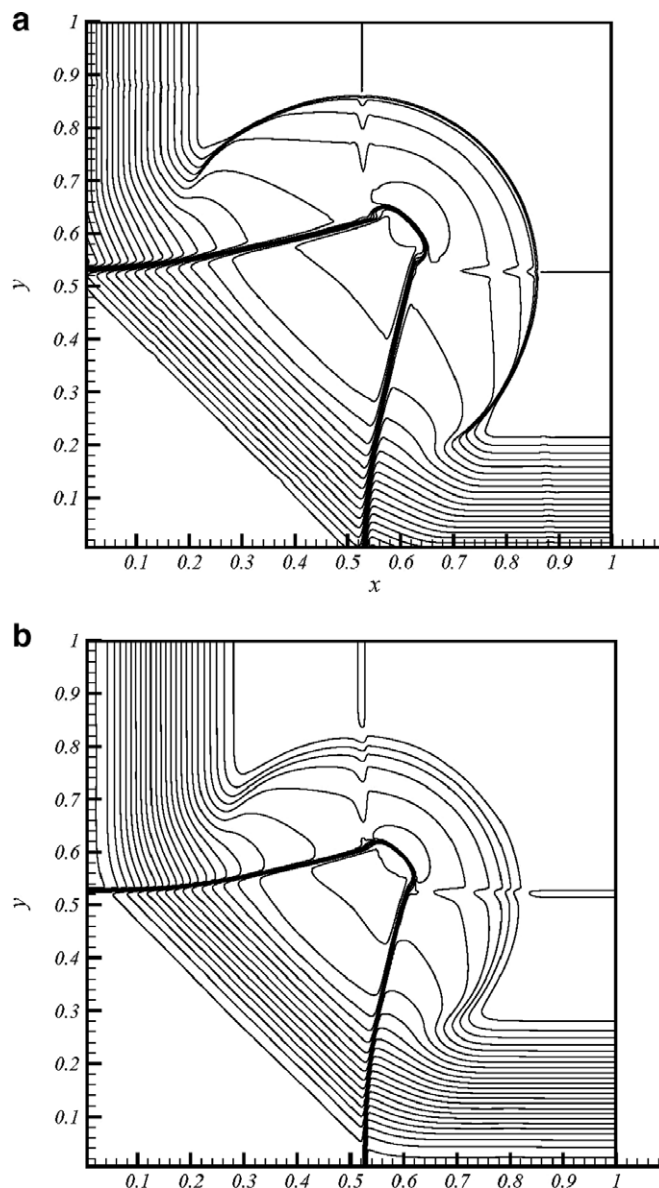


Fig. 22. Two-dimension Euler equations. Two-dimension Riemann problem. Configuration D.  $400 \times 400$  rectangular grid,  $CFL = 0.75$ ,  $t = 0.25$ . Density contour lines (25 contour lines: 0.51 to 0.99 step 0.02) (a) CWENO5 scheme, (b) “Superbee” limiter.

Fig. 21(a) shows the numerical results obtained with CWENO5 scheme, at  $t = 0.3$ . As one can see, the shock-waves are well resolved and the solution is symmetric. As in [17], the different types of Mach reflection are observed and the slip line that rolls up into a vortex along the symmetry line is visible.

In contrast, Fig. 21(b) shows the results obtained with the second-order TVD scheme (“Superbee” limiter), all the remaining parameters being unchanged. As one can see, the solution is more dissipated by the TVD scheme, this is especially true along the symmetry line.

*Configuration D:* interaction of rarefaction and contact waves.

The initial data are

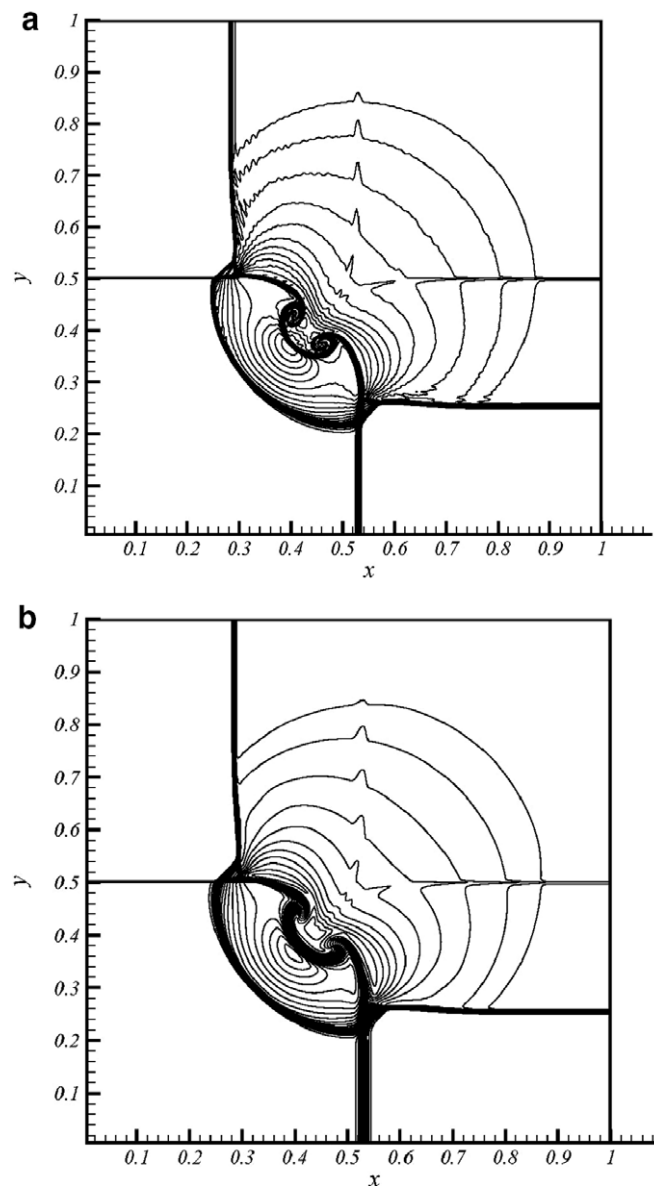


Fig. 23. Two-dimension Euler equations. Two-dimension Riemann problem. Configuration E.  $400 \times 400$  rectangular grid,  $CFL = 0.75$ ,  $t = 0.3$ . Density contour lines (34 contour lines: 0.55 to 1.21 step 0.02) (a) CWENO5 scheme, (b) “Superbee” limiter.

$$(\rho, u, v, p)^t = \begin{cases} (0.5197, 0.1, 0.1, 0.4)^t & \text{if } x > 0, y > 0, \\ (1, -0.6259, 0.1, 1)^t & \text{if } x < 0, y > 0, \\ (0.8, 0.1, 0.1, 1)^t & \text{if } x < 0, y < 0, \\ (1, 0.1, -0.6259, 1)^t & \text{if } x > 0, y < 0. \end{cases}$$

Fig. 22(a) shows the computed solution at  $t = 0.25$ .

The circular shock wave that bounds the subsonic area outside the rarefaction waves is clearly visible. The high resolution of these results is in close agreement with the corresponding results in [17]. Fig. 22(b) shows the results obtained with the TVD scheme: the circular shock-wave is more dissipated.

*Configuration E:* interaction of shock waves and contact discontinuities.

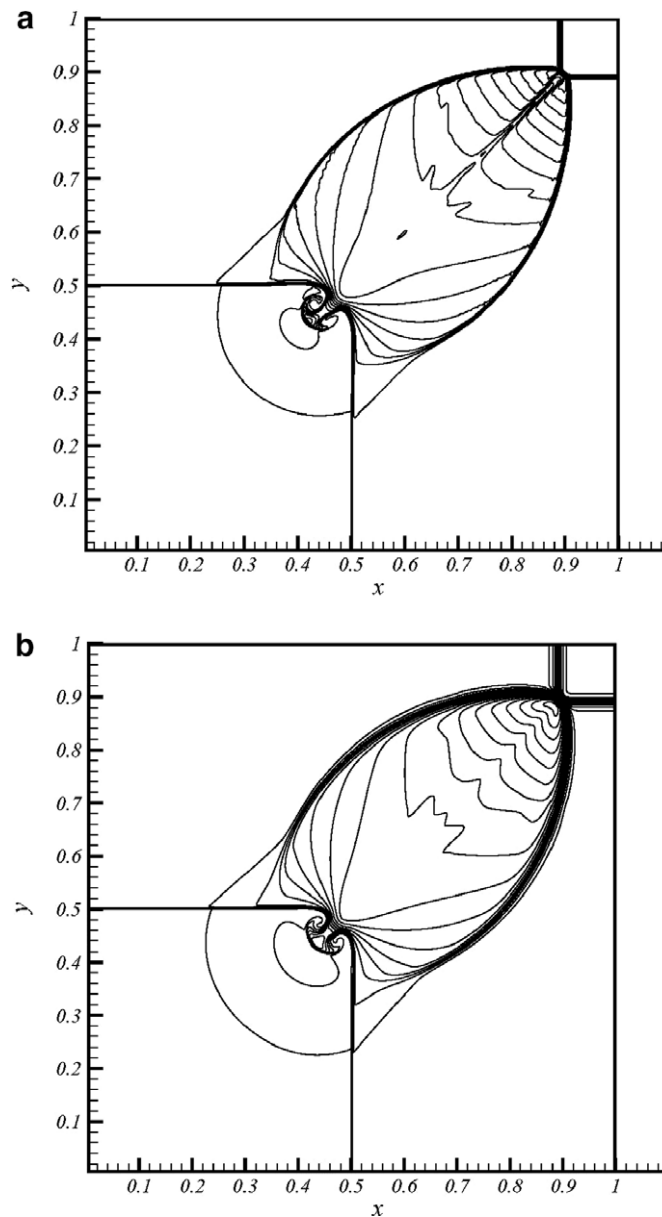


Fig. 24. Two-dimension Euler equations. Two-dimension Riemann problem. Configuration F.  $400 \times 400$  rectangular grid,  $CFL = 0.75$ ,  $t = 0.25$ . Density contour lines (30 contour lines: 0.54–1.70 step 0.04) (a) CWENO5 scheme, (b) “Superbee” limiter.

The initial data are now the following ones:

$$(\rho, u, v, p)^t = \begin{cases} (1, 0.1, 0, 1)^t & \text{if } x > 0, y > 0, \\ (0.5313, 0.8276, 0, 0.4)^t & \text{if } x < 0, y > 0, \\ (0.8, 0.1, 0, 0.4)^t & \text{if } x < 0, y < 0, \\ (0.5313, 0.1, 0.7276, 0.4)^t & \text{if } x > 0, y < 0. \end{cases}$$

Fig. 23(a) shows the computed solution at  $t = 0.3$ .

The slip lines which bend inside the subsonic area and end in spirals are clearly visible. Similarly, the oval shock wave that bounds the subsonic area is well predicted. This solution is in full agreement with [17], except for the oscillations behind the shock. Fig. 23(b) shows the results obtained with the TVD scheme: the spirals and the oval shock are more dissipated with such a scheme. The dissipative nature of the TVD scheme helps to damp the oscillations behind the shock.

*Configuration F:* interaction of shock waves and contact discontinuities.

The initial conditions are as follows:

$$(\rho, u, v, p)^t = \begin{cases} (0.5313, 0, 0, 0.4)^t & \text{if } x > 0, y > 0, \\ (1, 0.7276, 0, 1)^t & \text{if } x < 0, y > 0, \\ (0.8, 0, 0, 1)^t & \text{if } x < 0, y < 0, \\ (1, 0, 0.7276, 1)^t & \text{if } x > 0, y < 0. \end{cases}$$

Fig. 24(a) shows the results computed with CWENO5 reconstruction at  $t = 0.25$ . This solution is in close agreement with [17]. The slip lines that bend and end in spirals are clearly visible; the solution proposed by the VD scheme is more dissipative, Fig. 24(b).

Overall, our results based on the one-dimensional CWENO5 reconstruction, reveal the same detailed information on the variety of wave formations, in complete agreement with the results of Ref. [17]. Comparisons with a classical second-order TVD scheme indicate that the fine details of each interaction remain better captured with the CWENO5 reconstruction: clearly, this is the advantage of using a very high-order reconstruction.

However, one can note that the contact discontinuities are captured in the same way in using either a CWENO5 reconstruction or a TVD scheme.

The numerical results obtained with the second-order TVD scheme are in agreement with those obtained, for example, by Kurganov and Tadmor [22].

#### 4. Concluding remarks

In this paper, we constructed a new WENO interpolation procedure for 1D hyperbolic conservation laws; then, we straightforwardly extended this procedure to 2D configurations. This interpolation results from a convex centred combination of quadratic polynomials. Combined with a third-order TVD Runge–Kutta procedure for the time-integration, we proved that this procedure generates a fifth-order scheme in smooth regions and for small CFLs and remains essentially non-oscillatory near discontinuities.

The main advantage of the CWENO5 scheme is its possibility of treating the non-uniform meshes, without losing either its simplicity or its properties.

In addition, this scheme has some advantageous peculiarities.

Firstly, in the case of systems, it becomes possible to use a simple component-wise reconstruction without producing the inappropriate oscillations that generally appear with usual high-order schemes. In some cases, some slight oscillations may appear but they remain less significant than those produced by more classical component-wise reconstructions. Broadly speaking, the multidimensional extensions of the scheme show the same numerical behaviour.

Secondly, the numerical stability of the CWENO5 scheme is unaltered if one introduces highly varying source-terms in the equations; this point is significant, for example, in non-linear aero-acoustics where source terms must be incorporated into the equations if one wants to model non-linear regions of production of sound.



Lastly, the density constitutes a good sensor for the calculation of the smoothness indicators and preserves the ENO properties of the resulting scheme when one discretizes non-linear systems of equations. Once again, this result is advantageous since it makes it possible to simplify the reconstruction procedure.

With regard to the formulation of the parameter  $\varepsilon$ , the conclusions seem to be more contrasted. Indeed, this formulation does not bring anything new compared with the classical choice used in [2], when the solution is discontinuous. On the other side, when the solution is smooth, formula (27) produces results rather in good agreement with the theoretical analysis of Section 3: the convergence of the scheme is almost monotone and does not suffer from the “super convergence” phenomenon that sometimes appears with the use of a more classical parameter. For this reason, we think that the idea represented by formula (27) – although still perfectible – deserves to be preserved to improve the convergence properties of a WENO procedure. Maybe a local formulation of  $\varepsilon(u)$  would constitute a solution to improve the accuracy of the method in regions of smoothness close to a discontinuity.

To conclude, this new high-order scheme makes it possible to compute, with a good degree of accuracy, multi-scales problems containing discontinuities. Owing to its algorithmic simplicity and its robustness, this method can be regarded as a good basis for multidimensional extensions. However, preliminary results obtained in academic 2D configurations show that more work is needed to improve the capture of shock without generating spurious oscillations: a CWENO multi-dimensional reconstruction that enables to deal with curvilinear meshes, would possibly be suitable. This point will constitute the future direction of our work.

## Acknowledgment

The author wishes to thank with recognition, Dr. G.B. Deng (Ecole Centrale de Nantes – France), for having provided technical support essential for this work.

## References

- [1] A. Harten, B. Engquist, S. Osher, S. Chakravarthy, Uniformly high-order essentially non-oscillatory schemes, III, *J. Comput. Phys.* 71 (1987) 231–303.
- [2] C.-W. Shu, Essentially non-oscillatory and weighted essentially non-oscillatory schemes for hyperbolic conservation laws, in: Quarteroni (Ed.), *Lecture Notes in Mathematics*, Springer, Berlin, 1997.
- [3] J. Shi, C. Hu, C.W. Shu, A technique of treating negative weights in WENO schemes, *J. Comput. Phys.* 175 (2002) 108–127.
- [4] C. Hu, C.W. Shu, Weighted essentially non-oscillatory schemes on triangular meshes, *J. Comput. Phys.* 150 (1999) 97–127.
- [5] M. Dumbser, M. Käser, Arbitrary high-order non-oscillatory finite volume schemes on unstructured meshes, *J. Comput. Phys.* (2006), doi:10.1016/j.jcp.2006.06.043.
- [6] A.K. Henrick, T.D. Aslam, J.M. Powers, Mapped weighted essentially non-oscillatory schemes: achieving optimal order near critical points, *J. Comput. Phys.* 207 (2005) 542–567.
- [7] R. Fedkiw, Simplified discretization of systems of hyperbolic conservation laws containing advection equations, *J. Comput. Phys.* 157 (2000) 302–326.
- [8] D. Levy, G. Pupo, G. Russo, Compact central WENO schemes for multidimensional conservation laws, *SIAM J. Sci. Comput.* 22 (2000) 656–672.
- [9] A. Harten, P.D. Lax, B. Van-Leer, On upstream differencing and Godunov-type schemes for hyperbolic conservation laws, *SIAM Rev.* 25 (1983) 35.
- [10] C. Hirsch, *Numerical Computation of Internal and External Flows*, vol. 1, Wiley & Sons, 1987, pp. 371–401.
- [11] J. Casper, M.H. Carpenter, Computational considerations for the simulation of shock-induced sound, *SIAM Sci. Comput.* 19 (1998) 813–828.
- [12] Yu-X. Ren, M. Liu, H. Zhang, A characteristic-wise hybrid compact WENO scheme for solving hyperbolic conservation laws, *J. Comput. Phys.* 192 (2003) 365–386.
- [13] J. McKenzie, K. Westphal, Interaction of linear waves with oblique shock waves, *Phys. Fluids* 11 (1968) 2350–2362.
- [14] T.A. Zang, M.Y. Hussaini, D.M. Bushnell, Numerical computations of turbulence amplification in shock wave interactions, *AIAA J.* 22 (1984) 13–21.
- [15] C.-W. Shu, S. Osher, Efficient implementation of essentially non-oscillatory shock-capturing schemes, *J. Comput. Phys.* 77 (1988) 439–471.
- [16] Third Computational Aeroacoustics Workshop on Benchmark Problems, NASA/CP-2000-209790.
- [17] C.W. Schulz-Rinne, J.P. Collins, H.M. Glaz, Numerical solution of the Riemann problem for two-dimensional gas dynamics, *SIAM J. Sci. Comput.* 14 (6) (1993) 1394–1414.

- [18] C.W. Schulz-Rinne, Classification of the Riemann problem for two-dimensional gas dynamics, *SIAM J. Math. Anal.* 24 (1) (1993) 76–88.
- [19] J. Qiu, C.-W. Shu, On the construction, comparison and local characteristic decomposition for high-order central WENO schemes, *J. Comput. Phys.* 183 (2002) 187–209.
- [20] P. Woodward, P. Colella, The numerical simulation of two-dimensional fluid flow with strong shocks, *J. Comput. Phys.* 54 (1984) 115–173.
- [21] M. Brio, A.R. Zakharian, G.M. Webb, Two-dimensional Riemann solver for Euler equations of gas dynamics, *J. Comput. Phys.* 167 (2001) 177–195.
- [22] A. Kurganov, E. Tadmor, Solution of two-dimensional Riemann problems for gas dynamics without Riemann problem solvers, *Numer. Methods PDEs* 18 (2002) 548–608.